

This discussion paper is/has been under review for the journal Atmospheric Chemistry and Physics (ACP). Please refer to the corresponding final paper in ACP if available.

Discussion Paper | Discussion Paper

Discussion Paper | Discussion Paper | Discussion Paper | Discussion Paper

# Development and optimization of a wildfire plume rise model based on remote sensing data inputs – Part 2

R. Paugam<sup>1</sup>, M. Wooster<sup>1</sup>, J. Atherton<sup>1,2</sup>, S. R. Freitas<sup>5</sup>, M. G. Schultz<sup>3</sup>, and J. W. Kaiser<sup>4</sup>

<sup>1</sup>King's College London, Environmental Monitoring and Modelling Research Group, Department of Geography, Strand, London, WC2R 2LS, UK

<sup>2</sup>Department of Forest Sciences, University of Helsinki, Helsinki, Finland

<sup>3</sup>Institute for Energy and Climate Research-Troposphere (IEK-8), Forschungszentrum Jülich, Jülich, Germany

<sup>4</sup>Max Planck Institute for Chemistry, Mainz, Germany

<sup>5</sup>Center for Weather Forecasting and Climate Studies, INPE, Cachoeira Paulista, Brazil

Received: 17 January 2015 – Accepted: 2 March 2015 – Published: 31 March 2015

Correspondence to: R. Paugam (ronan.paugam@kcl.ac.uk)

Published by Copernicus Publications on behalf of the European Geosciences Union.

9815

## Abstract

Biomass burning is one of a relatively few natural processes that can inject globally significant quantities of gases and aerosols into the atmosphere at altitudes well above the planetary boundary layer, in some cases at heights in excess of 10 km. The “injection height” of biomass burning emissions is therefore an important parameter to understand when considering the characteristics of the smoke plumes emanating from landscape scale fires, and in particular when attempting to model their atmospheric transport. Here we further extend the formulations used within a popular 1D plume rise model, widely used for the estimation of landscape scale fire smoke plume injection height, and develop and optimise the model both so that it can run with an increased set of remotely sensed observations. The model is well suited for application in atmospheric Chemistry Transport Models (CTMs) aimed at understanding smoke plume downstream impacts, and whilst a number of wildfire emission inventories are available for use in such CTMs, few include information on plume injection height. Since CTM resolutions are typically too spatially coarse to capture the vertical transport induced by the heat released from landscape scale fires, approaches to estimate the emissions injection height are typically based on parametrizations. Our extensions of the existing 1D plume rise model takes into account the impact of atmospheric stability and latent heat on the plume up-draft, driving it with new information on active fire area and fire radiative power (FRP) retrieved from MODIS satellite Earth Observation (EO) data, alongside ECMWF atmospheric profile information. We extend the model by adding an equation for mass conservation and a new entrainment scheme, and optimise the values of the newly added parameters based on comparison to injection heights derived from smoke plume height retrievals made using the MISR EO sensor. Our parameter optimisation procedure is based on a twofold approach using sequentially a Simulating Annealing algorithm and a Markov chain Monte Carlo uncertainty test, and to try to ensure the appropriate convergence on suitable parameter values we use a training dataset consisting of only fires where a number of specific quality criteria are met, in-

9816

cluding local ambient wind shear limits derived from the ECMWF and MISR data, and “steady state” plumes and fires showing only relatively small changes between consecutive MODIS observations. Using our optimised plume rise model (PRMv2) with information from all MODIS-detected active fires detected in 2003 over North America, 5 with outputs gridded to a  $0.1^\circ$  horizontal and 500m vertical resolution mesh, we are able to derive wildfire injection height distributions whose maxima extend to the type of higher altitudes seen in actual observation-based wildfire plume datasets than are those derived either via the original plume model or any other parametrization tested herein. We also find our model to be the only one tested that more correctly simulates 10 the very high plume (6 to 8 km a.s.l.), created by a large fire in Alberta (Canada) on the 17 August 2003, though even our approach does not reach the stratosphere as the real plume is expected to have done. Our results lead us to believe that our PRMv2 approach to modelling the injection height of wildfire plumes is a strong candidate for inclusion into CTMs aiming to represent this process, but we note that significant 15 advances in the spatio-temporal resolutions of the data required to feed the model will also very likely bring key improvements in our ability to more accurately represent such phenomena, and that there remain challenges to the detailed validation of such simulations due to the relative sparseness of plume height observations and their currently rather limited temporal coverage which are not necessarily well matched to when fires 20 are most active (MISR being confined to morning observations for example).

## 1 Introduction to biomass burning plume injection heights

### 1.1 Background and motivation

Landscape scale vegetation fires, on average, burn an area equivalent to that of India plus Pakistan every year (Giglio et al., 2010). Such burning of vegetation converts 25 the bulk of the consumed biomass into trace gases and particulates, with typically rather little of the original mass remaining in the post-fire ash (Smith et al., 2005). The

9817

composition of the atmosphere is therefore greatly affected by this biomass burning (BB), with for example landscape fires being amongst the most dominant atmospheric sources of carbon monoxide, black carbon and organic aerosols, as well as a very important net source of  $\text{CO}_2$  through, for example, deforestation and peatland fires 5 (Kaiser et al., 2012; Ward et al., 2012). Chemical Transport Models (CTMs) are often used to study the large scale impacts of BB emissions, and many emission inventories have been developed to support such modelling. Because of the global distribution, but somewhat unpredictable and strongly varying nature of wildfire activity, the use of satellite Earth Observation (EO) data is generally required for the development of such 10 BB emissions inventories. Different methods exist to convert EO data into emission inventories, either based on (i) top-down approaches using inverse modelling and/or satellite-based retrievals of atmospheric trace gases such as CO (Gonzi and Palmer, 2010) or particulates (e.g. Aerosol Optical Depth; AOD Ichoku and Ellison, 2014), or (ii) bottom-up methods related to use of EO products more directly targeting fire on the 15 landscape, such as burned area (van der Werf et al., 2010) or Fire Radiative Power (FRP) (Kaiser et al., 2012).

Unlike most emissions to the atmosphere (apart from aircraft emissions or volcanic plumes), biomass burning is potentially able to loft and release its burden of gases and particles at various altitudes and not just at the surface. Because atmospheric transport is dependent on altitude, releasing smoke emissions at different heights into the atmosphere has a considerable influence on their region of impact, and may also alter their chemical evolution as, for example, the advection resulting from the interaction of the plume and the atmosphere can modify the ambient conditions within the developing plume (upon which its evolution in part depends). Examples of biomass burning 20 plumes reaching the high troposphere, or even the lower stratosphere, were first shown comprehensively by Fromm and Servranckx (2003), and subsequently the importance of the phenomena has been highlighted in several modelling studies (Turquety et al., 2007; Chen et al., 2009).

9818

As mentioned in the companion review to this work (Paugam et al., 2015), wildfire smoke plume dynamics span many different spatial scales, ranging from some millimetres around the flame where the heat is released primarily via the combustion of hot gases, to several meters when the plume interacts with the atmosphere creating turbulent mixing and the entrainment of ambient air in its core. Because all these dynamical processes cannot be resolved at the resolutions usually employed within CTMs ( $\gtrsim 100$  m), the plume dynamics and its associated vertical transport typically need instead to be parametrized (Colarco et al., 2004). The end product of such a parametrization is usually termed the “Injection Height” (InjH), defined as the height or the vertical layer in the CTM where smoke emissions associated with the observed/modelled fire are no longer controlled by the plume dynamics, and are therefore released into the ambient atmosphere. To more fully model the impact and fate of the emissions from landscape scale biomass burning, including for operational air quality or atmospheric composition forecasts, CTMs ideally require information on this InjH, as well as on the horizontal location, timing and quantity of the emissions themselves. However, at the global scale neither direct observations of InjH related information from satellite sensors (Kahn et al., 2008; Chen et al., 2009; Val Martin et al., 2010), nor InjH parametrizations used in models (Val Martin et al., 2012; Paugam et al., 2015), have been shown to provide satisfactory information. Plume-top height observations from spaceborne sensors such as the Multi-angle Imaging SpectroRadiometer (MISR), mounted onboard NASA’s Terra satellite, are available (Nelson et al., 2013), but they are generally relatively sparse, and are certainly not timely enough to be used operationally in CTMs targeting air quality early warning or the near real-time monitoring of atmospheric composition. Conversely current efforts on InjH predictions have only been able to substantially improve large scale plume transport relatively locally (Elguindi et al., 2010), or on single events (Dirksen et al., 2009). The purpose of our current work is to extend a popular current InjH parametrization scheme (Freitas et al., 2007), and optimise its parameters via comparison to MISR-derived plume height observations. The aim is to develop a more accurate parametrisation, suitable for near real-time implementation

9819

in a range of global-scale CTMs that aim to more accurately model biomass burning emissions evolution and transport.

## 1.2 Basic plume dynamics and EO observations

Since plume dynamics are highly coupled to atmospheric processes, the development and testing of a InjH parametrization that represents the vertical transport of the emitted material is a challenging task (Chen et al., 2009). Kahn et al. (2007) derived a simple 1-dimensional parametrization accounting for entrainment and buoyancy, but not moist convection (i.e. no cloud formation, no latent heat). Using MISR data processed to plume top height via a stereo-matching algorithm, sensitivity studies run for a single fire event were used to understand the implication of entrainment and fire temperature on the final InjH. Based on this approach, Kahn et al. (2007) outline the physical processes responsible of the vertical up-draft: the sensible heat flux or Convective Heat Flux (CHF) released by the fire, the fire size at the plume base, and the entrainment of ambient air. Kahn et al. (2007) also pointed out the potential effects of cloud physics and the importance of specifying the correct local ambient atmospheric conditions. The role of the atmosphere in smoke plume vertical transport is indeed central and two-fold, both acting against the buoyancy triggered by the initial CHF (via entrainment), and also enhancing the plume rise as the ambient cooling favours water vapour condensation and thus the release of latent heat. In certain scenarios, the latent heat release is such that it can accelerate the vertical up-draft considerably, “pushing” the plume up to the stratosphere where the material contained within it can be released (Fromm et al., 2010). To this non-exhaustive list of the factors controlling the final plume InjH, subsequent studies have added the wind drag (Freitas et al., 2010), the number of cores within the plume (Liu et al., 2010), and the number of initial Cloud Condensation Nuclei (CCN) (Reutter et al., 2013). Several parametrizations taking into account some or all of these influences already exist, and have been implemented in various air quality models and CTMs (see Goodrick et al., 2013; Paugam et al., 2015, for reviews). Among these, three make reference: (i) the 1-dimension off-line cloud Plume

9820

Rise Model (PRM) developed by Latham (1994) and later by Freitas et al. (2007, 2010); (ii) the turbulent-convective flux based on the Eddy Diffusivity Mass Flux scheme (pyro-EDMF; hereafter) derived by Rio et al. (2010), (iii) and the empirical/dimensional approach of Sofiev et al. (2012).

The prerequisites required to initialize these three plume rise models are generally information on fire size (usually the “active fire area” that denotes the area of active fuel consumption and fire energy emission), the Convective Heat Flux (CHF), along with the ambient atmospheric conditions (i.e. stratification, and also relative humidity when microphysical processes are considered). While the host CTM, or global reanalysis atmospheric model, can be used to extract the ambient atmospheric profiles at the fire location, satellite remote sensing data is generally required to characterize the active fire area (AF-area), which equates to the surface area of a black body having the same spectral emission properties as does the observed fire at the measurement wavebands (Dozier, 1981). Furthermore, as described for example in Paugam et al. (2015), fire radiative power (FRP) products can be used to estimate CHF via the ratio between radiant and convective heat release.

The Moderate-resolution Imaging Spectroradiometer (MODIS) sensor, operated on the Aqua and Terra satellites, can provide multispectral observations from which the FRP and AF-area of the detected fires (and individual fire pixels) can be derived. Since MODIS and MISR are both available on the Terra satellite, it is relatively easy to obtain collocated active fire and smoke plume height information. Indeed, a large number of fire events are available with such information, for example via the MISR plume height project<sup>1</sup>. These data have already been used for the optimization and evaluation of various plume rise parametrizations, for example Sofiev et al. (2012) and Val Martin et al. (2012). However, as mentioned in Paugam et al. (2015), CHF, AF-area and plume top height information extracted from simultaneously recorded MODIS and MISR observations do not take into account the time delay between the characteristics of the causal fire and those of the plume top, which maybe importance since the height to which

<sup>1</sup><https://www-misr.jpl.nasa.gov/getData/accessData/MisrMinxPlumes/>

smoke ascends will be related to the fire characteristics present when that plume was initially produced, and not necessarily to the fire characteristics at the time the plume has reached neutral buoyancy. They also typically do not consider the potential effects of absorption of the emitted fire radiance by the plume itself, which might result in erroneous fire activity measures. For these reasons, the selection of matched fire characteristics and plume top height observations needs to be done carefully when collecting data for the formulation and evaluation of plume Injh parametrisations. Ideally there should be a focus on remotely sensed observations that best represent a “steady state” situation with regard to both the causal fire and the resultant plume, avoiding situations where (i) the plume is potentially masking parts of the driving fire, or (ii) where the fire and plume are too close to their initialisation times and thus still changing their nature, or too near to their end point where plume and atmospheric dynamical processes can be too highly coupled. The current work takes account of these issues, making careful use of simultaneously recorded fire and plume observations to try to minimise the effect of these issues, whilst remaining focused on the development and performance evaluation of the wildfire plume rise model of Freitas et al. (2007). This PRM model is the most attractive for use as it has the largest range of physics built in (i.e. micro-physical and wind shear effects), though its performance is still debated, since the last comparison with MISR-derived plume top height data showed rather poor agreement (Val Martin et al., 2012).

In this study, we enhance the Freitas et al. (2007) PRM by improving (i) the dynamics of the model, with more physical constraints in terms of entrainment and detrainment; (ii) the conservation of mass; and (iii) the estimation of CHF from FRP observation. Furthermore, we aim at delivering an improved approach to the PRM performance evaluation, by being very selective when identifying suitable MODIS- and MISR-derived datasets, e.g. screening the MISR data set to extract only those events where we consider both the fire and the plume are at a mature stage of their evolution. Our manuscript is structured as follows: Sect. 2 derives the equations used within our enhanced version of the Freitas et al. (2007) PRM (which we term here PRMv2). Sec-

tion 3 presents methodologies to derive fire activity information, which are then used in Sect. 4 to define a robust dataset used for the model optimization and performance evaluation dataset. In particular Sect. 4 lists the selection criteria used to extract only fire events that we consider to be in a “steady state”. Section 5 introduces the optimization procedure used to derive the new input parameters of PRMv2, and presents the results of the performance evaluation based on example of stable and unstable atmosphere. Section 6 illustrates a first attempt to build a climatology of landscape-scale InjH for North America, based on the newly optimised PRMv2, whilst the final Section draws together the conclusions from the work, and discusses possible future developments.

## 2 Plume Rise Model (PRM) derivation

### 2.1 Past versions: PRMv0 and PRMv1

A detailed description, together with an overview of recent developments of the Freitas et al. (2007) PRM used herein are reported in Paugam et al. (2015). The original version, PRMv0, is described in detail in Freitas et al. (2007) and Freitas et al. (2010) and is a 1-dimensional plume model based on the original formulation of Latham (1994), containing equations for vertical momentum, the first thermodynamic law and the continuity of water phases that are solved explicitly. Freitas et al. (2007) and Freitas et al. (2010) assume the wildfire to cover a circular area on the Earth surface, with homogeneous fire characteristics defined by (i) CHF, derived as a fraction of the total heat released (following experimental work of McCarter and Broido, 1965), and (ii) AF-area derived using the WF-ABBA Geostationary Operational Environmental Satellites (GOES) product (Wild Fire Automated Biomass Burning Algorithm Prins et al., 1998). While the AF-area used within PRMv0 was based on these remotely sensed data from GOES, the total heat released was not estimated from the EO data, but instead a prescribed heat release range was used varying with vegetation type (e.g. 30 to 80 kW m<sup>-2</sup> for tropical

9823

forest). The cloud physics within PRMv0 is based on a simple micro-physical module counting 3 hydrometeors (cloud,rain,ice). The horizontal momentum is parametrized through two entrainment coefficients modelling the effect of (i) the turbulence at the edge of the stack (Freitas et al., 2007) (ii) and the drag caused by the ambient wind shear (Freitas et al., 2010). Finally, in PRMv0 the plume top height was defined as the altitude where the vertical velocity falls below 1 m s<sup>-1</sup>. During operations, the PRMv0 model is run twice for each extreme of the prescribed total heat release range, and InjH defined as the layer set between the two model run outputs. While PRMv0 provided some reasonable results when compared with a very high resolution 3-D plume rise model ATHAM (Freitas et al., 2010), comparisons of PRMv0 injection heights with MISR-derived plume top height datasets have not been so convincing (Val Martin et al., 2012).

In an attempt to improve the performance of PRMv0, we previously derived a scheme to estimate both AF-area and CHF from satellite EO data (Val Martin et al., 2012; Paugam et al., 2015). This new version, PRMv1, kept the PRMv0 model core, but the initialization module was modified to accept both CHF and AF-area information, in this case both derived from MODIS observations. The ability to relate CHF to an almost directly observable variable (i.e. FRP, which is a standard product from MODIS Justice et al., 2002), rather than estimating it indirectly from land cover type, was anticipated to potentially bring significant advantages. Furthermore, since MODIS pixels have a significantly smaller ground footprint than do GOES pixels, the AF-area estimates derived from them are expected to be more reliable than from GOES (Giglio and Justice, 2003; Giglio and Schroeder, 2014). Finally, in PRMv1 we were also able to define the final InjH as a single altitude, given by the modelled plume top height, rather than as the midpoint of range of plume height estimates. One limitation introduced by use of MODIS data in PRMv1 is, however, that unlike the very frequently updated data provided by GOES (Xu et al., 2010), MODIS provides observations only a few times per day for any particular fire, cloud cover permitting. PRMv1 was applied in the work of Val Martin et al. (2012), where it was referenced as the “dual-band” method due to the fact that

9824

data from two different wavebands of MODIS data are used in the derivation of AF-area using the Dozier (1981) algorithm. When compared with MISR data however, the correlation of the PRMv1 model InjH results and MISR-derived plume top height remained low, and with a slope of the linear best fit lower than 0.5 (Val Martin et al., 2012).

## 2.2 Improved plume-atmosphere interactions: PRMv2

The processes involved in plume dynamics are dependent upon ambient atmospheric conditions (e.g. entrainment, wind shear), and therefore on altitude. In the boundary layer, entrainment and wind shear act against the buoyancy, while for plumes that make it to the free troposphere, if entrainment, wind shear and stratification are still a break to the residual buoyancy, the ambient cooling can generate latent heat via condensation of the entrained water vapour and therefore potentially re-accelerate plume rise. Combining all these effects, the detrainment of the plume in the atmosphere is most certainly happening at all altitude levels (Kahn et al., 2007). To account for more complex plume-atmosphere interactions, we have now further modified the PRMv1 model to handle horizontal mass exchange. To do so, the quantity  $\zeta = \rho R^2$  is introduced as a prognostic variable, with  $R(z)$  the radius of the plume and  $\rho(z)$  the air density. Even though the horizontal flow is still parametrized, the plume mass is now resolved, together with momentum and energy conservation. Figure 1 introduces the system variables and the effect of the lateral flow parametrization, while the equations are described in Appendix A.

PRMv2 formulation is based on 4 prognostic variables  $\zeta$ ,  $w$  (vertical velocity),  $T$  (temperature), and  $u$  (horizontal plume velocity) following

$$\partial_t w + w \partial_z w = \frac{1}{1+\gamma} g B - \epsilon w^2, \quad (1)$$

$$\partial_t T + w \partial_z T = -w \frac{g}{c_p} - \epsilon w(T - T_e) + (\partial_t T)|_{\text{micro}}, \quad (2)$$

$$\partial_t \zeta + w \partial_z \zeta = -\zeta \partial_z w + w \zeta(\epsilon - \delta), \quad (3)$$

9825

$$\partial_t u + w \partial_z u = -\epsilon w(u - u_e), \quad (4)$$

where  $g$  is the acceleration due to gravity,  $c_p$  the specific heat at constant pressure, and  $\gamma = 0.5$  is the virtual mass coefficient introduced by Simpson and Wiggert (1969) (see Appendix A for more details). Together with this system of equations, PRMv2 also

includes an equation for passive scalar transport. Given a mixing ratio  $\phi$ , a passive tracer is advected following

$$\partial_t \phi + w \partial_z \phi = -\epsilon w(\phi - \phi_e) \quad (5)$$

For each variable  $x(z)$ ,  $x_e(z)$  stands for the ambient value. At each time step, assuming that the air pressure within the plume equals the ambient pressure,  $\rho$  is evaluated using the ideal gas law,  $\rho = \frac{\rho_e}{R T}$ , with  $R = 286.9 \text{ J kg}^{-1} \text{ K}^{-1}$  the perfect gas constant, and  $R$  the radius of the plume is computed from  $R = \sqrt{\zeta/\rho}$ .

The en/de-trainment coefficients are inspired from shallow convection parametrizations (Gregory, 2001; Pergaud et al., 2009) and parametrized using a set of 4 parameters ( $C_\epsilon$ ,  $C_\delta$ ,  $C_{\epsilon,\text{dyn}}$ ,  $C_{\delta,\text{dyn}}$ ) (see Appendix A for more details) such that,

$$\epsilon = \max \left( 0, C_\epsilon \frac{B}{w^2} \right) + C_{\epsilon,\text{dyn}} \frac{1}{w} \frac{du}{dz} \quad (6)$$

$$\delta = \max \left( 0, C_\delta \frac{B}{w^2} \right) + C_{\delta,\text{dyn}} C_{\epsilon,\text{dyn}} \frac{1}{w} \frac{du}{dz} \quad (7)$$

The microphysical scheme of the model remains unchanged from PRMv0 of Freitas et al. (2007). To account for the effects of latent heat (e.g.  $(\partial_t T)|_{\text{micro}}$  in Eq. 2), four mixing ratios are transported for water vapour and the three hydrometeors cloud, rain and ice.

The PRMv2 model is run on a 100m resolution vertical grid, reaching a maximum altitude of  $z^{\text{max}} = 20 \text{ km}$ , with an adaptive time step calculated to respect the Courant–Friedrich–Lowy stability criterion, with an upper limit of 5s (Freitas et al., 2007). To

9826

- close the system of Eqs. (1)–(5), (i) boundary conditions are set to no slip at  $z = 0$  (i.e.  $u(z = 0) = 0$ ) and are open at the top, (ii) and ambient atmospheric profiles of pressure  $p_e$ , temperature  $T_e$ , humidity  $r_e$ , and horizontal wind velocity  $u_e$  are taken from European Centre for Medium-range Weather Forecasts (ECMWF) analysis data.
- 5 Furthermore, as in Freitas et al. (2007) to take into account the flow singularity near the land surface, the vertical velocity ( $w(z = 0) = w_0$ ) and the temperature ( $T(z = 0) = T_0$ ) are evaluated from the analytical model of Morton et al. (1956). Knowing the plume radius  $R_0$  and the CHF, a virtual source height  $z_v = \frac{5}{6}\alpha^{-1}R_0$  is derived and  $w_0$  and  $T_0$  are defined as

$$10 \quad w_0 = \frac{5}{6\alpha} \left( \frac{0.9\alpha F}{z_v} \right)^{1/3}, \quad (8)$$

$$T_0 = T_e(z = 0) \left[ 1 + \frac{5}{6\alpha} \frac{F}{g} \frac{z_v^{-5/3}}{(0.9\alpha F)^{1/3}} \right], \quad (9)$$

where  $F$  is the buoyancy flux defined by  $F = \frac{g R_{\text{CHF}}}{\pi c_p p_e(z=0)}$  and  $\alpha$  is the entrainment coefficient of the Morton et al. (1956) model.

According to energy budget measurements conducted on small-scale vegetation fires, convection represents around half of the total energy released during the combustion process (McCarter and Broido, 1965), and radiation around 10% (Freeborn et al., 2008). This yields the relation  $\text{CHF} = 5\text{FRP}$ , which is the formula used in the initialisation scheme of PRMv1. However, these measurements were conducted on laboratory-scale fires, and the energy budgets of landscape scale fires may be different, particularly as flame structure can change dramatically with fire properties. For example, short flames can have a low spectral emissivity at wavelengths outside of the  $\text{CO}_2$  and  $\text{H}_2\text{O}$  emission bands, but longer flames with path lengths exceeding 5 m appear to demonstrate black body-type behaviour (Johnston et al., 2014). In PRMv2, a new parameter  $\beta$  has therefore been introduced to adjust for such potential variations

9827

in energy partitioning, and CHF is defined as

$$\text{CHF} = \beta \text{FRP}. \quad (10)$$

With the above definitions, the PRMv2 model is fully defined with the inputs of (i) AF-area ( $R_0 = \sqrt{\text{AF-area}/\pi}$ ) and fire radiative power (FRP), (ii) local ambient atmospheric profile at the fire location, and (iii) a set of 6 parameters: 4 for the en-de/trainment scheme ( $C_e$ ,  $C_\delta$ ,  $C_{e,\text{dyn}}$ ,  $C_{\delta,\text{dyn}}$ ) and 2 for the initialization module ( $\alpha$  and  $\beta$ ).

The end point of the time integration ( $t_{\text{end}}$ ) is controlled by the variation of the dry air mass in the plume,  $M_p = \int_{z=0}^{z_{\text{max}}} \zeta dz$ . When the mean of the relative variation of  $M_p$  over the last 10 time steps is lower than  $2 \times 10^{-5}$ , the plume is considered to be in a steady state, and the relative entrainment ( $M_{\text{entr}}$ ) and detrainment profiles ( $M_{\text{detr}}$ ) to fire activity (i.e. injected mass) can be determined from the ratio of the time integration of the entrained and detrained mass flux ( $\pi e \zeta w$  and  $\pi \delta \zeta w$ ) and the injected mass at the base of the plume.

$$M_{\text{entr}}(z, t = t_{\text{end}}) = \frac{dz \int_{t'=0}^{t_{\text{end}}} e(z) \pi \zeta(z, t') w(z, t') dt'}{\int_{t'=0}^{t_{\text{end}}} \pi \zeta(0, t') w(0, t') dt'} \quad \frac{[\text{kg}]}{[\text{kg}]} \quad (11)$$

$$15 \quad M_{\text{detr}}(z, t = t_{\text{end}}) = \frac{dz \int_{t'=0}^{t_{\text{end}}} \delta(z) \pi \zeta(z, t') w(z, t') dt'}{\int_{t'=0}^{t_{\text{end}}} \pi \zeta(0, t') w(0, t') dt'} \quad (12)$$

However, as  $M_{\text{entr}}$  and  $M_{\text{detr}}$  are dependent on the time integration,  $t_{\text{end}}$ , and as the few snapshots available from MODIS every day cannot provide fully accurate information on the fires temporal evolution, to simplify the integration of PRMv2 into CTMs the final InjH is defined as the altitude layer where detrainment  $M_{\text{detr}}/M_{\text{detr}}^{\text{max}} > 0.5$  and where there is the highest net detrained mass  $M_{\text{detr}}(z) - M_{\text{entr}}(z)$ . This InjH altitude is hereafter denoted  $\text{InjH}_{\text{PRMv2}}$ , whilst the plume top (e.g. for comparison to MISR-derived values) is defined as the top of the InjH layer, denoted  $\text{InjH}_{\text{PRMv2}}^{\text{top}}$ . An example of a PRMv2

9828

result for the fire O13289-B39-P3 of the MISR-derived data set of (Nelson et al., 2013) is shown in Fig. 2. The following Sect. 3 explains how the AF-area and FRP are derived from the EO data for use in PRMv2, whilst Sect. 4 presents the robust compilation of a set of fire and plume observables, and Sect. 5 describes the method used to estimate values for the models remaining 6 parameters.

### 3 Sub-pixel active fire information: FRP, temperature and active fire area

As mentioned in Sect. 2.2, the PRMv2 initialization module requires information on the sub-pixel active fire characteristics. As in PRMv0 and PRMv1 (see Sect. 2.1), AF-area is used as an estimate of the plumes basal radius  $R_0$ , over which the convective flux estimated from the FRP measurement is being homogeneously released. This section presents the approaches used to derive FRP and AF-area, and the methodology developed to estimate the atmospheric transmittance which is required in both FRP and AF-area derivation.

#### 3.1 Atmospheric transmittance

To adjust the measured radiances for atmospheric effects, we computed the atmospheric transmittance for each fire and waveband of observation, which is particularly important when combining multispectral information to retrieve fire parameters, such as when using the Dozier (1981) algorithm. Using ECMWF vertical profile data on atmospheric temperature, water vapour and pressure, the MODTRAN atmospheric radiative transfer model (Berk et al., 2006) was run to estimate the spectral distribution of atmospheric transmittance  $\tau'_\lambda$  at the location and time of the fire, with the assumption of a fixed atmospheric GHG profile and a rural aerosol (23 km visibility). For MODIS' middle and thermal infrared (MIR and TIR) measurement wavebands, the effective band-integrated atmospheric transmittance  $\tau$  was calculated via the convolution of the

9829

spectral response function (SRF)  $f_{\text{srif}}$ :

$$\tau = \frac{\int f_{\text{srif}}(\lambda) \tau'_\lambda(\lambda) d\lambda}{\int f_{\text{srif}}(\lambda) d\lambda} \quad (13)$$

#### 3.2 The Dozier algorithm implementation

We used an iterative solver to provide solutions to the Dozier (1981) dual-band equations fed with observations from MODIS' MIR and TIR bands, using this system to derive the effective AF-area, as well as the fire-effective kinetic temperature  $T_f$  (Giglio and Schroeder, 2014). We used the formulation of the Dozier (1981) dualband algorithm used in Giglio and Kendall (2001) and Wooster et al. (2005):

$$\frac{L_i}{\tau_i} = pB(T_f, \lambda_i) + (1 - p)\frac{L_{b,i}}{\tau_i} \quad \text{for } i = 1 (\lambda \in \text{MIR}), \text{ and } i = 2 (\lambda \in \text{TIR}) \quad (14)$$

where a fire emissivity of one in both MIR and TIR wavelength ( $\epsilon_{f,i} = 1$ ) is assumed, and where  $L_i$  is the observed spectral radiance in waveband  $i$  of wavelength  $\lambda_i$ ,  $B$  is the Planck function,  $L_{b,i}$  is the “background” spectral radiance estimated from neighboured pixels, and  $\tau_i$  is the atmospheric transmittance of the band  $i$  defined by Eq. (13),  $p$  is the proportion of the pixel covered with thermally emitting fire components (e.g. flaming and smouldering areas of combustion), so that if  $A_{\text{pixel}}$  is the pixel area, AF-area is therefore AF-area =  $pA_{\text{pixel}}$ .

Equation (14) was originally implemented with 1 km spatial resolution (at nadir) data from the Advanced Very High Resolution Radiometer (AVHRR), and later applied to 4 km GOES (Prins et al., 1998) and to 370 m Hotspot Recognition Sensor (HSRS) data collected by the bi-spectral Infrared Detection Experimental Small Satellite (BIRD) (Wooster et al., 2003; Zhukov et al., 2006). Giglio and Kendall (2001) show that “dualband” retrievals become potentially unusable when fire fractional areas ( $p$ ) fall below 0.005, due primarily to the difficulty in isolating small fire signals in the TIR band, and (Giglio and Schroeder, 2014) indicates that as a result only around seven percent of

9830

MODIS active fire pixels actually provide meaningful AF-area retrievals. Analysis of significantly coarser spatial resolution GOES imagery results in a even smaller proportion of fires having meaningful retrievals, which is why we avoid use of GOES or other geostationary data here. Instead we focus on MODIS, and maximised the ability of the dual-band algorithm to derive useful information by clustering groups of spatially contiguous active fire pixels into single “fires”, whose mean MIR and TIR band spectral radiances are then used as the algorithm inputs. This active fire pixel clustering approach prior to application of the Dozier (1981) dualband algorithm was originally used by Wooster et al. (2003) and Zhukov et al. (2006) with multispectral HSRS data collected by the BIRD Small Satellite, and Peterson et al. (2013) recently used a similar method with MODIS data. The clustering minimises impacts from band-to-band non-co-registration offsets (Shephard and Kennelly, 2003), though at the cost of a loss in the spatial fidelity of the effective active fire temperature (Giglio and Schroeder, 2014). However, since in the PRMv2 initialization scheme we only use the AF-area output of the Dozier (1981) dualband algorithm, this loss of spatial fidelity in effective fire temperature has no significant impact.

It is important to note that the fire cluster information as derived from the Dozier (1981) dualband algorithm represents everything in the selected fire pixel clusters that are above the assumed background temperature, and for example  $T_f$  cannot be interpreted in terms of the true “fire temperature” (Giglio and Schroeder, 2014). Within the MODIS pixel footprint ( $\geq 100 \text{ ha}$ ), there very likely exists a mix of flaming, smouldering and/or cooling areas, which are all emitting more energy per unit area than the ambient background (see Eq. 14). Since the CHF responsible for the plume rise is mainly triggered by the intense energy release associated with the flaming zone (Wooster et al., 2003), we developed a filter to minimise the impact of the smouldering/cooling areas on the Dozier (1981) retrievals. Assuming lower sub-pixel effective fire temperatures are more likely to be from pixels dominated by smouldering activity, we first run the Dozier algorithm at pixel level (as in Giglio and Schroeder, 2014). We select only pixels with Dozier (1981) retrievals that we consider valid (i.e.  $100 < T < 1500 \text{ K}$  and  $\text{AF-area} > 0$ ),

9831

and that have high sub-pixel fire effective temperatures ( $T > 600 \text{ K}$ ). We cluster these pixels into individual fires, and finally run the Dozier (1981) algorithm a second time on each cluster. This filter is referenced hereafter as the “low sub-pixel temperature” filter, and the threshold of  $600 \text{ K}$  was selected such that mainly pixels at the edge of the raw MODIS cluster were removed (which are more likely to contain high amounts of smouldering activity and cooling ground, behind the main fire front). We note that with regard to FRP derivation using the MIR radiance method of (Wooster et al., 2003), this already minimises the FRP contribution of “cooling” (but not smouldering) areas below  $650 \text{ K}$  as described in that work. It is true that this filter could possibly erroneously impact clusters whose pixels are covered with small fraction of the fire front head, but we consider that this will have less effect that including large areas of smouldering ground within the Dozier (1981) retrieval. Furthermore, since the input parameters of the model PRMv2 (see Sect. 2.2) are optimized to fit our fire/plume observations (see Sect. 5), the threshold temperature for the filter does not need to be particularly well constrained, although it is important that it lies towards the upper range of what is smouldering activity.

To improve the convergence of Dozier (1981) algorithm, we follow Peterson et al. (2014) and add an extra test on the TIR radiance signal, deselecting all filtered clusters with  $\Delta_{11} = L_2 - L_{b,2} < 0.5 \text{ W m}^{-2} \text{ str}^{-1}$ . A detailed evaluation of our implementation of the Dozier (1981) algorithm, including a comparison of results from fires simultaneously observed by MODIS and BIRD HSRS, is reported in Appendix B.

### 3.3 FRP derivation

This section introduces two independent methods to derive FRP, based on the outputs of the Dozier (1981) algorithm ( $\text{FRP}_{\text{doz}}$ ) or on the single band approach of (Wooster et al., 2005,  $\text{FRP}_{\text{mir}}$ ). As described in detail in Wooster et al. (2005),  $\text{FRP}_{\text{mir}}$  is directly derived from the MODIS MIR band observations assuming that (i) around fire temperature ( $\sim 700 \text{ K}$ ) the Planck function in the MIR behaves as a quadrature function (i.e.  $B(\lambda_{\text{MIR}}) = a T_f^4 \quad \forall T \sim 700$  with  $a$  being sensor specific; see Table 1 Wooster et al., 2005), and (ii) that the spectrally integrated emissivity of the fire is similar to its emis-

9832

sivity in the MIR ( $\epsilon_f \sim \epsilon_{f,MIR}$ ). Using previous notation,  $FRP_{mir}$  is then defined as

$$\begin{aligned} FRP_{mir} &= A_{pixel} p \sigma \epsilon_f T_f^4 = A_{pixel} \frac{\sigma \epsilon_f}{a \epsilon_{f,MIR}} p \epsilon_{f,MIR} B(\lambda_{MIR}, T_f) \\ &= A_{pixel} \frac{\sigma}{a} \frac{L_{MIR} - L_{b,MIR}}{\tau_{MIR}} \end{aligned} \quad (15)$$

where  $\sigma$  is the Stefan–Boltzmann constant and where the last derivation uses Eq. (14)

- 5 applied to the MIR band with the assumption that fires are usually smaller than the pixel size, so that  $(1 - p) \sim 1$ . Following the derivation of  $FRP_{mir}$ ,  $FRP_{doz}$  is defined using the output from the Dozier algorithm and assuming that the fire is a black body ( $\epsilon_f = 1$ )

$$\begin{aligned} FRP_{doz} &= AF\text{-area } \sigma T_f^4 \quad \text{if } T_f > T_b \\ &= 0 \quad \text{if } T_f = T_b \end{aligned} \quad (16)$$

- 10 Note here that we do not remove the contribution of the background as in Peterson et al. (2013). Indeed as shown in Eq. (15),  $FRP_{mir}$  is defined as the radiation emitted by the surface covered by the fire, without removal of the background contribution covering the same surface. However following its definition  $FRP_{mir}$  switches to 0 when the fire temperature is equal to the background temperature. The same switch is applied to the
- 15 definition of  $FRP_{doz}$ .

#### 4 Datasets used for PRMv2 optimisation and performance evaluation

This section describes how the dataset containing fire characteristics (AF-area and FRP), ambient atmospheric condition, and observed plume top height is computed. It is based on the same fire and plume observations made by MODIS and MISR contained

- 20 in the official MISR plume injection height project (Nelson et al., 2013), except that we now add an estimate of AF-area to each selected fire (one which tries to minimise impacts from the cooling ground behind the active fire front), provide an “observed” InjH

9833

from the MISR-derived plume top height information in order to remove atmospheric transport effects, and derive a new FRP for each fire by adjusting the observed value for atmospheric transmittance effects and the influence of “cooling ground”.

##### 4.1 Selecting a representative plume-fire-atmosphere dataset

###### 5 FRP and active fire area

As in Sofiev et al. (2012) and Val Martin et al. (2012), our database used for the PRMv2 model optimisation and evaluation was based on the MISR-derived plume height dataset derived with the MINX software described in (Nelson et al., 2013). Instead of using the MODIS active fire information provided in the MINX-derived database however,

- 10 we re-extracted the relevant data from the original MODIS Active Fire (MOD14) products (Justice et al., 2002) such that definition of the active fire pixels relevant to each plume remains unaffected by the exact delineation of the plume contour used in MINX (Val Martin et al., 2012). Using the algorithms described in the previous section, we derive AF-area and FRP for each clusters where flaming activity is dominant (i.e.
- 15 application of the low sub-pixel temperature filter). Furthermore, we required fire clusters to have a mean TIR band spectral radiance signal  $\Delta_{11} > 0.5 \text{ W m}^{-2} \text{ str}^{-1}$  in order to improve the convergence characteristics of our dualband algorithm implementation.

We used the MINX-derived smoke plume contour reference point for the plume location, and applied our methodology to every MODIS active fire cluster found within

- 20 a radius of 20 km. If more than one fire cluster was present, the cluster with the largest AF-area was selected for inclusion in the database as this was considered to be the most likely cause of the observed plume.

###### Plume injection height

As mentioned previously, a good proxy for InjH is the final altitude of the smoke plume.

- 25 Previous studies using products from the MINX-MISR plume height project (Val Martin

et al., 2010; Sofiev et al., 2012) have defined InjH as the maximum height returned by MISR within the MINX-identified plume contour. However, at the time of the MISR observation the retrieved plume heights are not just representative of the current status of the fire, but have also been influenced by the fires development over the previous tens of minutes (or even perhaps hours; depending on the length of the plume and the ambient winds). Further influences come from local atmospheric dynamics, such as e.g. orographic waves. To minimise the impact of such effects on the dataset, Val Martin et al. (2012) defined InjH as extracted from MISR plume heights as the maximum of the plume height distribution calculated from the MISR pixels within a distance of 10% of the active fire cluster radius. We use a similar approach, defining a zone where we expect the plume to remain unaffected by horizontal atmospheric transport (hereafter called the plume “stack”) using the pixel height variation along the plume length (see Fig. 3). Using pixel heights distributed according to their distance to the fire cluster (within bins of 1.5 km), we considered the plume stack to stop where the local maximum plume height falls below 25 % of the stack height maximum, which was dynamically calculated when moving away from the cluster location. An example of the horizontal extension of the stack is shown in Fig. 3, see red zone of the bottom plot.

The top of the stack ( $h^{\text{stack}}$ ) was then defined as the mean of the binned local maximum height within 20 % of the maximum stack height (see red points in the bottom plot of Fig. 3).

Figure 4 shows a comparison of the stack height  $h^{\text{stack}}$  and the original plume top height  $h^{\text{plume}}$  as defined in the MISR plume height product. Plumes where the relative difference between  $h^{\text{stack}}$  and  $h^{\text{plume}}$  exceeds 70 % were removed from the database, and we notice that this situation appears primarily associated with plumes attached to multiple separate fire clusters. We deal here only with scenarios where a plume is linked to a single fire cluster, but in any case this filtering removes only 4.0 % of the original MINX MISR dataset. Considering the 3632 remaining fires, Fig. 4 shows that the new definition of the stack top does not introduce a bias, since we see an almost one-to-one relation between  $h^{\text{stack}}$  and  $h^{\text{plume}}$  (slope of 0.95). The new definition of  $h^{\text{stack}}$

9835

is rather an adjustment on a per fire basis, providing slightly updated interpretation of plume height.

Together with  $h^{\text{stack}}$ , we introduce a measure of the InjH layer based on an alternative definition to previous approaches since PRMv2 is able to solve the vertical detrainment from the plume, and thus not only provides the final plume top height (as for PRMv1), but also vertical profile. We therefore define InjH as a detrainment zone, using the vertical height distribution of the pixels contained in the stack. Using a 500 m vertical step, we define a density distribution of pixel height  $\gamma_h$ , and define InjH as the layer contained between the highest local maximum of  $\gamma_h$  and the highest retrieved height. Figure 2a shows the distribution  $\gamma_h$  for the stack shown in Fig. 3. As MISR is only able to observe the plume top, the above definition of the InjH layer is only weakly constrained by the MISR-derived data, and will be used as such in the following Sections. That is, we believe our definition of InjH [which is correlated to  $h^{\text{stack}}$ , not shown] is more representative of the fires evolution, and more likely linked with the coincident measures of CHF and AF-area that we are able to derive simultaneously than is the MISR-derived  $h^{\text{stack}}$ .

### Atmospheric profile

We use ECMWF analysis runs to define, for each fire cluster, ambient atmospheric profiles of pressure, temperature, humidity and wind, re-sampled to a 1.0° resolution horizontal grid. The vertical mesh of the ECMWF analysis contains 60 levels before the 1 February 2006, and 91 levels thereafter, with similar vertical resolution near the ground ( $\sim 10$  m) gradually stretched up to the top of the domain located at 65 and 80 km for the 60 and 91 level grids, respectively. In addition, we also use the diagnostics from the forecast runs of ECMWF (0.25° resolution, ECMWF, 2012) to estimate the boundary layer height ( $h^{\text{BL}}$ ) and the total column water vapour (TCWV) at each fire location.

9836

## 4.2 Fire selection for the match-up database

Based on the different definitions of FRP, AF-area and plume height mentioned previously, 3 separate match-up datasets were defined.

1. the “raw fire cluster” MISR dataset, which is based on the original MINX-derived plume height  $h^{\text{plume}}$ , showing a “good” quality flag. Here, FRP and AF-area were derived from direct application of the Dozier algorithm to MODIS fire clusters, without use of the low sub-pixel temperature filter or TIR signal test. Hereafter they are named FRP’ and AF-area’, respectively. However, the same fire cluster location selection as described in previous Section was used in cluster selection close to the vicinity of the plume. This dataset covers 3313 fires.
2. the “filtered fire cluster” MISR dataset, which is based on the previous data set with full application of the methodologies for FRP, AF-area and stack height  $h^{\text{stack}}$  determination described in the previous section. This dataset covers 1992 fires.
3. the “Good” cluster dataset, which include FRP, AF area and InjH layer as defined in previous section. It is specifically developed for the optimization of the PRMv2 model and detailed below.

To further maximise the appropriateness and quality of the match-up “fire-atmosphere-plume height” dataset used to optimize and evaluate the PRMv2 model, in addition to the criteria of the filtered fire cluster MISR dataset, the following requirements were also set in the good fire data set:

- The rejection of fires on agricultural land, since these are often quite small, controlled fires with very changeable characteristics caused by human intervention, and which may therefore be less likely to reach a steady state. According to the MISR data set land cover map shown in Paugam et al. (2015), after removal of agricultural fires, the remaining fires are located either on extra tropical forest or on savannah land cover types.

9837

- A correct match between the wind information extracted from the ECMWF analysis and from the MISR products. The stereo-matching algorithm used in MINX corrects for plume displacement, and each pixel in the MISR plume height product is characterized by a plume top height and local wind speed across and along the plume direction (Nelson et al., 2013). Using all pixels from the MINX-contoured plume, and the same vertical resolution as the ECMWF atmospheric profile, we derived a new wind profile with associated errorbars from the MISR observations (see triangular points in Fig. 5). Plumes with less than 3 points in their profile were rejected, and a correct match only accepted if the lowest residual errors between the MISR- and ECMWF-derived wind profiles were below an arbitrary threshold of 50, estimated empirically from multiple comparisons. The residual error is derived to account both for wind and wind gradient, and is defined as

$$\text{residual} = \sum_{\forall k \in \text{profile}} \left[ \frac{u_h^{\text{ECMWF}} - u_h^{\text{MIRS}}}{u_h^{\text{ECMWF}}} \right]_k^2 + \left[ \frac{\nabla u_h^{\text{ECMWF}} - \nabla u_h^{\text{MIRS}}}{\nabla u_h^{\text{ECMWF}}} \right]_k^2 \quad (17)$$

where  $u_h^X$  the amplitude of the horizontal wind profile  $X = \text{ECMWF}$ , or  $\text{MISR}$ . See Fig. 5 for examples of matching and non-matching profiles. It is important to note that this criteria indirectly filters out fire events occurring on complicated terrain, since the misrepresentation of terrain effects is a common reason for large scale atmospheric models deviating from observations. It also removes smaller plumes, and therefore indirectly but preferentially smaller fires, since profiles must have 3 or more points to be valid. The MISR flag and the wind profile tests together remove a large proportion (76%) of the plumes within the initial MINX-MISR dataset.

- A limited number of fire clusters near the plumes origin. Only plumes with less than 5 fire clusters within a 30 km radius around the reference location (set in the MINX-derived contour plume) are selected. This removes another 13% of the MISR-derived plumes.

9838

- A plume is clearly visibly observable. The objective here is to remove fires that fail to show a well developed plume, possibly because it is too early in the fires lifetime. Each fires plumes development was assessed using simulated true colour composite MODIS imagery covering 100 km around each fires location, and to be considered valid the MODIS imagery had to have at least one pixel within the MISR plume mask brighter than a pre-defined threshold (thus signifying the present of a plume). In future, the MODIS cloud product might be usable in this context. This condition predominately filters out smaller fires, and another 4 % of the MINX-MISR plumes were removed by its application.
- Using the selection criteria outlined above, the MINX-MISR dataset was reduced to 192 fires. Finally, MISR nadir-view imagery was used to perform a final visual inspection of the remaining fire plumes, to ensure that no cluster except the one located near the reference point was potentially affecting the matching plume. After this final check, a set of 39 matched fire and plume observations remained for used in PRMv2 model optimisation and evaluation.

As mentioned previously, and in Paugam et al. (2015), it is important for our work that the matched plume and fires were in relative steady states because, as shown by the simulations of Trentmann et al. (2006), the plume needs time to adjust to changes in the causal fires characteristics. In the ideal situation of a fire of constant heat release modelled by Trentmann et al. (2006), the fire plume required 40 min to reach a steady state. Real fires can change their characteristics over quite short time-scales, and also fire activity varies strongly over the diurnal cycle (Roberts et al., 2009). Since plume dynamics are highly non-linear, it is difficult to estimate the time delay between a change in fire characteristics and those in the resultant plume, and thus to understand when fire and plume activity are time synchronised. Furthermore, when a fire is growing, its plume typically increases in size and the stack may increasingly fill with large particulates released by the fire, which can increase the scattering and/or blocking of the fire-emitted MIR wavelength radiation (Kahn et al., 2007; Paugam et al., 2015). In situations of low ambient wind, where the stack can remain above the fire, where only

9839

one observation of the fire exists it is difficult to estimate the proportion of the emitted MIR radiation that might be affected. To try to understand how the fire and plumes are linked at the time of the MISR overpass, we used multiple overpasses of the Terra and Aqua satellites to build a more comprehensive story of FRP and plume structure for individual fires. For each of the previously 39 selected fires, for every overpass we examined MODIS simulated true colour and Near-Infra Read (NIR) colour ( $R = 2.15 \mu\text{m}$ ,  $G = 1.24 \mu\text{m}$ ,  $B = 0.6 \mu\text{m}$ ) composite imageries. Figure 6 shows an example, illustrating the time evolution of the fire O18779-B36-P1 of the MISR dataset (see Supplement Figs. S7–S45 for the time evolution of all fire from the good cluster dataset). For fires located at higher latitudes, more than two overpasses (1 Terra +1 Aqua) are typically available, and for some fires we found up to 7 cloud-free overpasses.

The NIR colour composite provides qualitative information about both the fire and the plume, providing an insight to the plumes relative location with respect to the fire, to the plumes constituent make-up (e.g. ice vs. water droplets). In the case of the fire O18779-B36-P1, since detected active fire pixels only appear on the edge of a large iced fluffy cloud, either the cloud mask in the MODIS fire product is masking the plume as cloud and preventing detection of fire pixels underneath, and/or the plume is absorbing or scattering enough of the fires MIR radiation to limit the number of fire pixels detected. Looking at the 21:50 UTC MODIS image closely, we can see that the plume has extended southwards and blocked the detection of fire in a region where only 10 min ago in the last observation fire pixels were detected with the MODIS MYD14 product (Aqua observation). Only one of our 39 match-up fires showed this type of obvious fire masking, and we believe that this will be more common in the case of large fires with plumes containing larger particles, and where the ambient wind speed is relatively low. Under such conditions, the MIR and TIR radiance signals from the fire maybe underestimated by different amounts, yielding an underestimated FRP (and therefore CHF), and an increased uncertainty in AF-area. We removed this single fire from our match-up database, leaving a total of 38 discrete fire events, and note that in such dense plumes with a strong TIR signature InjH could probably instead likely

9840

be estimated by matching the TIR brightness temperature and ambient atmospheric temperature profiles (Smith and Platt, 1978).

### 4.3 Fire-plume-atmosphere interactions

To understand some of the interaction between plume and fire behaviours, Fig. 7 shows for the 3 datasets introduced in previous section the relationships between the different fire and plume observables, namely FRP, AF-area, FRP density defined as

$$Q_r = \frac{\text{FRP}}{\text{AF-area}} [\text{kW m}^{-2}], \quad (18)$$

and plume height ( $h^{\text{plume}}$ ,  $h^{\text{stack}}$  depending of the dataset).

As in Val Martin et al. (2010) and Amiridis et al. (2010), we separate fires into two classes according to the stability of the ambient atmosphere. Following the definition of Val Martin et al. (2010), we consider the atmosphere as stable if at the height  $z = z^{s_{\max}}$  of the first maximum of the stability  $s = \frac{\partial \theta}{\partial z}$ ,  $s(z^{s_{\max}})$  is  $1 \text{K km}^{-1}$  greater than for the 3 layers above and below, and/or  $1.5 \text{K km}^{-1}$  greater than 6 layers above and below. Together with the 38 fires of the good cluster dataset (bottom row of Fig. 7i–k), fire and plume observables are also reported for the raw fire clusters (top row, plot a–c) and the filtered fire clusters (middle row, plot d–f) MISR dataset introduced in previous section.

Considering only plumes above the boundary layer ( $h^{\text{stack}}$  or  $h^{\text{plume}} > h^{\text{BL}} + 0.25 \text{ [km]}$ , red circle in 2 first columns of Fig. 7), the raw clusters data set show a higher correlation between  $\text{FRP}'$  and  $h^{\text{plume}}$  for the unstable than stable atmosphere situations. This is similar to the findings presented by Amiridis et al. (2010) for eastern European agricultural fires, and Val Martin et al. (2010) who used an early version of the dataset used herein, and supports the prior findings of Lavoué et al. (2000) who demonstrated a direct relationship between fire activity and plume height. However, as in Amiridis et al. (2010) and Val Martin et al. (2010), we show that this behaviour only holds in cases where atmospheric stratification is weak. The main modification in our raw cluster dataset when compared with the earlier dataset used by Val Martin et al. (2010),

9841

are (i) a selection of the MODIS fire cluster based on the full MOD14 product and not only the fire pixels reported in the MINX output, and (ii) and an extra 755 events totalling 3813 fires from which we only conserve 3313 where the Dozier (1981) algorithm converges. The final number of plumes located above the PBL and which occur in an unstable atmosphere is 148, compared to 32 in Val Martin et al. (2010), resulting in a lower correlation between  $h^{\text{plume}}$  and  $\text{FRP}'$  (0.4 compared to  $\sim 0.5$  for Val Martin et al., 2010), and a lower slope of the log-log relationship, decreasing from 0.2 for Val Martin et al. (2010) to 0.08 here.

The filtered clusters data set (Fig. 7d–f) shows similar fire-plume behaviour as does the raw clusters dataset. Even if FRP is now derived from cluster formed of only “hot” fire pixels ( $> 600 \text{ K}$ , see Sect. 4.1) and plume height is based on the new definition of  $h^{\text{stack}}$ , the relationship between fire and plume observables hold, and even show better features as the fire characteristics are now more independent Peterson et al. (2014).

The good clusters dataset contains only 4 fires with an unstable atmosphere, amongst which 3 reach the free troposphere (red circle in Fig. 7j). However the previous relationship between  $h^{\text{stack}}$  and FRP seems to hold, showing a strong correlation of 0.9 even when including one fire which stays trapped in the PBL. Although the sample number is low, the effect of the atmospheric stability seems to be consistent and therefore appears to establish a good test for the validation of plume rise models.

## 20 5 PRMv2 optimization and evaluation

### 5.1 Optimization of PRMv2 parameters

#### 5.1.1 Optimisation approaches

The variables contained within the PRMv2 model parameter vector ( $d = [\alpha, C_e, C_\delta, C_{e,\text{dyn}}, C_{\delta,\text{dyn}}, \beta]$ ) were defined in Sect. 2. To estimate the optimum value of each of these parameters we used two related but distinct metropolis-type algorithms, a Sim-

9842

ulated Annealing (SA Kirkpatrick et al., 1983) and an adaptive Markov Chain Monte Carlo method (McMC Braswell et al., 2005) to: (i) identify the optimal parameter vector,  $d$ , capable of delivering physically representative observations of plume injection height; and (ii) run a model sensitivity analysis to estimate the uncertainties of  $d$  with regards to the MISR-derived InjH observations.

We used an objective function ( $f$ ) to quantify the misfit between the InjH simulations and observations. The same form of  $f$ , the residual sum of squares, was used in both SA and McMC, selected to depend only on the top of the InjH layer, in order to avoid over-constraining the system since the measure of the InjH layer thickness is less robust than is its maximum height (see Sect. 4.1). MISR-derived injection height “observations” ( $y^{\text{obs}} = \text{InjH}_{\text{obs}}^{\text{top}}$ ) were compared to the simulated injection heights output from PRMv2 ( $\hat{y} = \text{InjH}_{\text{PRMv2}}^{\text{top}}$ ):

$$f(y^{\text{obs}}, d, \text{args}) = \sum_{\text{obs}} \left[ a^{R,\text{corr}} (\hat{y}(d, \text{args}) - y^{\text{obs}}) \right]^2 \quad (19)$$

where  $\hat{y}(d, \text{args})$  is obtained from the PRMv2 model run with input of the vector parameter  $d$  and the arguments args: FRP, AF-area, and local atmospheric profiles (see Sect. 2.2),  $y^{\text{obs}}$  is derived from the MISR data set as explained in Sect. 4.1, and  $a^{R,\text{corr}}$  is a correction term to prevent the plume radius  $R$  diverging too greatly.  $a^{R,\text{corr}}$  is defined such that if the relative variation of  $R$  between the base of the plume and the first model level  $\Delta R_{z=0} = \frac{R(z_1) - R(z_0)}{R(z_0)}$  exceeds a threshold of 200, then  $a^{R,\text{corr}} = 10\Delta R_{z=0}$ , otherwise  $a^{R,\text{corr}} = 1$ .

Although related by their shared use of the Metropolis criterion (Metropolis et al., 1953), SA and McMC are fundamentally different algorithms generally applied for different purposes. SA is used primarily to find a single set of optimum parameter values ( $d$ ) given some observations, whereas McMC is used to assess parameter value uncertainty. In SA the probability of acceptance ( $P_{\text{accept}}$ ) of a new parameter vector ( $d_{\text{new}}$ ),

9843

knowing its current vector ( $d_{\text{current}}$ ) is defined as

$$P_{\text{accept}} = \min \left( 1, e^{-\frac{1}{2} \frac{\Delta E[f(d_{\text{new}}), f(d_{\text{old}})]}{T}} \right) \quad (20)$$

where  $\Delta E$  is the gain of the likelihood function, which is a function of the objective function evaluated with both old and new parameter values. If  $P_{\text{accept}}$  is greater than or equal to unity, then the new innovation is accepted since the sum of the square of the residuals have fallen to a lower value. If  $P_{\text{accept}}$  is smaller than unity, then  $P_{\text{accept}}$  is compared to a random number drawn from a uniform distribution  $U \sim [0, 1]$ . In this way, the SA algorithm has the chance to escape local minima by temporarily accepting less good parameter innovations in the search for the values that minimise the objective function globally. In addition, the probability value (chance of escape from local minima) is a function of the temperature  $T$ , which is decreased according to a cooling schedule from which SA gets its name. As the algorithm converges to the assumed minima, the cooling schedule dictates that fewer “bad” moves are accepted. Finally, some cessation criterion is activated (e.g. number of iterations or minimum temperature) to accept the “best guess” of the parameter vector,  $d$ .

We used the SA algorithm to first assess the physical representativeness of the observed fire plumes modelled by PRMv2. Several instances of SA were run with different training data sets  $\mathcal{D}^{\text{learning}}$ , achieved by sampling a sub-set of 20 fires randomly selected among the 38 fires of the good clusters data set whose selection was detailed in Sect. 4. The instances were subsequently initiated with randomly selected starting points  $d_0$  in the prior parameter range (see Table 1). On completion of the SA runs, the residuals for individual fires were analysed, and we identified fires whose plumes were physically not well represented by PRMv2. SA was used in preference to McMC for this step since it is less computationally demanding.

After running the SA algorithm, we used an adaptive McMC algorithm to analyse the error of the optimal vector,  $d$ , within a Bayesian probability framework. The aim was to recover the joint posterior probability distribution of the model parameters that contains information relating to both the optimal parameter values and their uncertainty, and is

9844

learned from the measured observations ( $y^{\text{obs}}$ ). McMC numerically solves Bayes law for the model parameters,  $d$ , which can be stated as:

$$P(d|y^{\text{obs}}) \propto P(y^{\text{obs}}|d) \times P(d) \quad (21)$$

where  $P(d|y^{\text{obs}})$  is the joint posterior probability of the parameters.  $P(y^{\text{obs}}|d)$  is referred to as the likelihood of the observations and is where the physical model enters the equation and  $P(d)$  is the prior distribution of parameters. Posterior probability distributions for individual parameters are referred to as marginal distributions, and are used to calculate uncertainty bounds (credible intervals) and optimal values (for example expectations or modes). Flatter, dispersed distributions represent more uncertainty with respect to a particular parameter. In contrast tighter, peaked distributions mean that a parameter is well constrained by the available observations. Correlations between parameters are used to reveal structural inefficiencies in the underlying physical model, and can be found by analysing the joint distributions.

$P(y^{\text{obs}}|d)$  is formulated by assuming that each measurement is corrupted by an identically and normally distributed error term that is parametrised by zero mean and an estimate of error variance,  $s^2$  which represents the inherent error in each observation.  $s^2$  is estimated from try and error to allow McMC to scan the parameter space with an acceptance rate  $R_{\text{accept}}$  remaining above 30% (Gelman et al., 2000). The likelihood,  $P(y^{\text{obs}}|d)$ , is the product of the probability of each measurement given the current parameter guess,  $d$ :

$$P(y^{\text{obs}}|d) = \prod_{\text{all obs.}} \frac{1}{\sqrt{2\pi s^2}} \exp\left(\frac{-[\hat{a}^{R,\text{corr}}(\hat{y}(d, \text{args}) - y^{\text{obs}})]^2}{2s^2}\right) \quad (22)$$

In practice, the log transform of the likelihood is used. This renders Eq. (22) as a sum rather than a product over the observations, and thus facilitates the introduction of the objective function,  $f$ , into the likelihood term ( $\log P(y^{\text{obs}}|d) = \text{constant} - \frac{1}{2s^2} f(y^{\text{obs}}, d)$ ).

9845

For most non-trivial cases, it is not possible to analytically solve 21. McMC are a class of algorithms that address this by sampling from a *proposal* distribution. If properly selected, enough samples from the proposal distribution can be used to approximate the target posterior distribution. We provide only a brief explanation of the McMC algorithm used here, for full details see Braswell et al. (2005). McMC proceeds by first sampling a new parameter from the proposed distribution. The ratio of the likelihood of the old parameter vector to the new parameter vector is then used for the metropolis step, where “less good” guesses can be accepted by comparison to a uniform random number. Unlike SA there is no cooling schedule, which leaves the McMC algorithm free to sample the posterior distribution, rather than focusing on a single set of parameter values, as in SA.

A particular obstacle to using the McMC method is finding an optimal proposed distribution for selecting new parameter values. If this distribution is poorly tuned, then the ratio of accepted to rejected parameter values becomes too low, and the chain (samples) does not properly converge to the stationary distribution. The Braswell et al. (2005) algorithm is an adaptive method that automatically tunes the proposal distribution during the initial stages of the run, based on the “acceptance ratio”. Once tuned, the chain needs to be run for several thousand iterations; long enough to properly sample the posterior distribution.

20 For PRMv2, we used McMC to compute the joint posterior distribution of the parameter space. 68% Credible Intervals (CI, analogous to, but not the same as, Frequentist confidence intervals) for marginal parameter distributions were calculated and the correlations between the parameters analysed. Prior to this analysis, we had little knowledge of the expected parameter values, with the exception of knowing reasonable parameter bounds. Uniform bounded priors were used for all parameters, with the central value of the prior distribution selected as the initial guess for the distribution.

### 5.1.2 Optimisation results

A total of 32 instances of SA were run, of which 53% (17 fires) ended with a sum square residual error lower than  $20[m^2]$  ( $\sim$  median error of the 32 instance). Two fires were frequently found that had large residual error values. One, O29627-B39-P1, showed in 5 Aqua MODIS imagery collected just 10 min after the MISR overpass a neat alteration of the plume becoming brightener just above the fires location, which could come from contamination of neighboured clouds being advected above the fire, or from the growth of the plume itself (see Supplement Fig. S28). In this case, it is difficult to understand precisely the plumes evolution. However, it is clear that at the time of the MISR imagery 10 the plume is not in a steady state. The other O24457-B42-P2 showed the formation of a pyro-cumulus cloud 1:45 h after the MISR overpass (see Supplement Fig. S22). As PRMv2 is able to converge for most of the remaining 36 test fires, we assumed that the model physics are robust enough, and removed these 2 outliers from our analysis. The sum square residual error (Eq. 19) calculated from the full 36 fire data-set (i.e.  $f^{all}$ ) was 15 derived for each 17 vector parameter associated with “low”  $f$ , and the optimal vector parameter  $d_{SA}$  selected as the vector with the lowest  $f^{all}$  (see Table 1). Comparison of  $d_{SA}$  with parameter values used in en/detrainment schemes of shallow convection (Gregory, 2001; Pergaud et al., 2009; Chikira and Sugiyama, 2010) is difficult as our formalism is slightly different (e.g. momentum source at ground level generated by 20 the fire, entrainment coefficient including wind shear effect, see Appendix A for more details). However it is interesting to see that the value of the entrainment coefficient  $C_e$  is  $\sim 3$  times larger than typical value used in shallow convection, e.g. Chikira and Sugiyama (2010) used 0.6 while Pergaud et al. (2009) used 0.55. In the configuration 25 of fire plume, high velocities at ground level create an extra source of momentum and simultaneously decrease the entrainment as  $\propto \frac{1}{w}$  (see Eq. 6). Therefore a higher value of  $C_e$  is necessary to balance changes in vertical velocity. Now, when a air parcel moves upwards, its dynamics switches gradually from velocity dominated to buoyancy dominated (similar to natural convection) which according to Chikira and Sugiyama

9847

(2010) requires a lower value of  $C_e$ . In the current approach however,  $C_e$  keeps the same value along the plume. Future development of PRMv2 would investigate the implementation of en/de-trainment coefficients varying with altitude and/or momentum source strength.

5 Considering the entire InjH layer (not only its top height), Fig. 8 shows an almost one-to-one relationship between the MISR-derived observations and the PRMv2 simulations using the parameter vector  $d_{SA}$  for all 38 fires selected in Sect. 4.2. An excellent match between modelled InjH and Observed InjH is present for all fires, except the two outliers discussed above where the simulated InjH appears significantly overestimated, 10 perhaps because the morning MODIS overpass occurred towards the initial stage of the fire when the plume is still building up and adjusting to the increasing fire activity. The sparse information we have, (2 snapshots) are insufficient to confirm this. In any case, the optimised PRMv2 parameters developed in Sect. 2 are clearly able to deliver InjH simulations that are very well matched in most cases to the MISR-derived plume 15 height estimates of the good cluster dataset defined in Sect. 4.

To further validate PRMv2, as well as to study its sensitivity to the input parameters, we used the Markov chain Monte Carlo (McMC) uncertainty test, introduced in Sect. 5.1.1. The diagnostics from this can be found in the Supplement (Figs. S1–S3). The McMC algorithm was run for over 20 000 iterations with an observation error  $s^2$  of 20 30, allowing the acceptance rate  $R_{accept}$  to remain in the range 36–47%. Although  $s^2$  is representative of the inherent error in the observations, in this study we used trial and error to estimate this value. We originally ran the McMC algorithm with smaller  $s^2$  values ( $< 0.5$ ), however the algorithm failed to converge resulting in a poor sampling of the posterior distribution. It is unclear as to whether the successful value is a precise 25 representation of the observation error, so we rather used the posterior distribution as an exploratory tool to assess correlations between parameters and the sensitivity of the model to individual parameters. With the exception of the reported marginal intervals and modes, we refrained from making detailed predictions of uncertainty using the full posterior distribution, which we show in Fig. 9.

9848

The marginal parameter distributions  $d_{\text{McMC}}$  (see diagonal plots of Fig. 9) are used to derive the 68% interval (shaded area in diagonal plots of Fig. 9) listed in Table 1. The off-diagonal plots of Fig. 9 display the cross-correlation of the 6 parameters, in particular showing that:

- 5 –  $\alpha$  and  $C_e$  are anti-correlated, which makes sense as the initial up-draft  $w_0$  is inversely proportional to  $\alpha$  (Eq. 8) such that if  $\alpha$  increases, the updraft is weaker and less entrainment (i.e.  $C_e$ ) is necessary to slow down the plume rise,
- 10 –  $C_{\text{dyn},e}$  and  $C_{\text{dyn},\delta}$  are anti-correlated, this is due to the dependence of  $\delta_{\text{dyn}}$  to  $\frac{1}{w}$ ,  $C_{\text{dyn},e}$ , and  $C_{\text{dyn},\delta}$  (Eq. A8). When  $C_{\text{dyn},e}$  increases, mass in the plume increases and  $w$  decreases. As  $C_{\text{dyn},e}$  and  $C_{\text{dyn},\delta}$  are anti-correlated, this shows that even if the mass increases,  $C_{\text{dyn},\delta}$  increase is not necessary to control mass detrainment, and even acts against it. The formulation of the dynamic detrainment should be revised in the future, since the presence of  $C_{\text{dyn},e}$  is certainly unnecessary (i.e. large 68% credible intervals).
- 15 –  $C_e$  and  $\beta$  are correlated for the same reason as  $\alpha$  and  $C_e$  are anti-correlated. Indeed,  $\beta$  controls the initial updraft while  $C_e$  is responsible of the break. Those 2 parameters are the most sensible.

It is interesting to note that the parameter vector found via SA ( $d_{\text{SA}}$ , purple lines in Fig. 9) is in the range of the credible intervals of  $d_{\text{McMC}}$ . When only considering the 36 fires (i.e. with the two outliers of Fig. 8 removed), the two approaches deployed here (SA and McMC) are independent. Their convergence therefore supports the legitimacy of our optimization procedure. During subsequent application of the PRMv2 model, we decided to use the parameter vector  $d_{\text{opt}}$ , defined by the mode of the posterior  $d_{\text{McMC}}$  (see Table 1), because the marginal modes represent an optimal guess based on a thorough exploration of the parameter landscape (posterior), whereas the SA represented a point guess defined by arbitrary stopping criteria.

9849

## 5.2 PRMv2 model performance evaluation

Due to the limited number of observations that came out of our match-up dataset selection criteria (see Sect. 4.2), the relative lack of information on the exact match between fire and plume dynamics, and the potential alteration of the fire-emitted MIR signal by certain of the plumes, we could only use 36 fires in our parameter optimization procedure (Sect. 5.1). To help evaluate the set of optimised parameters  $d_{\text{opt}}$ , we therefore ran the “tuned” PRMv2 model on a year of MODIS observations of North American fires (latitude = 35–70° N, longitude = 40–170° W), checking whether the modelled plume heights are able to reproduce the observed physical behaviour, in particular the dependence to the atmospheric stability originally highlighted by Val Martin et al. (2010) and Amiridis et al. (2010) and described in Sect. 4.3.

Using the Collection 5 MODIS active fire product (Giglio et al., 2003), for each detected fire pixel we ran the fire clustering algorithm detailed in Sect. 4.1 and computed FRP and AF-area for each fire with the procedures detailed in Sect. 3. Along with simulation of the plumes using the optimised PRMv2 model, we also ran the previous versions of PRM (PRMv0 and v1) and the plume injection height parametrization of Sofiev et al. (2012) for this dataset. While PRMv0, PRMv1 and the Sofiev et al. (2012) parametrizations were run for every detected fire where the Dozier (1981) algorithm converges (i.e. 30 951 fires), PRMv2 was only run for the 19 804 fires which verify the low sub-pixel temperature filter and the TIR radiance signal test introduced in Sect. 3.2.

Following the results of Fig. 7, which shows the relationship between observed plume height and FRP for stable and unstable atmospheres, Fig. 10 shows the relationship between FRP and modelled plume injection height for plumes recorded as being above the boundary layer for the three versions of PRM used here, as well as the Sofiev et al. (2012) parametrization.

PRMv2 is the only approach that produces behaviour similar to those of the observations, i.e. with a power law relationship ( $h = a \text{FRP}^k$ ) for scenarios with unstable atmospheres that (i) has an exponent of the same order of magnitude ( $k \sim 0.1$ ) and (ii)

9850

exhibits a stronger correlation than when fires in stable atmospheres are considered. Furthermore, PRMv2 is also the only approach that predicts a non-negligible number of fires with an InjH top above 8 km (see Table 2). Although PRMv2 seems able to better represent the type of extreme plume heights caused by Pyro-Cumulonimbus (PyroCbs) formation, it does not yet match the full extent of the plume heights reported in Fromm et al. (2010), who for 2002 detailed a total of 17 PyroCbs with a top plume height in the range 9.5–13.0 km. However, these observed heights are for the entire plume, including far downwind of the source fire, whilst our models simulate only the height of the stack closely located above the causal fire (Sect. 4.1). Since plume dynamics are highly coupled to atmospheric transport, distal plume heights can be significantly affected by ambient physical processes. A complete evaluation of PRMv2 with respect to such downwind plume top height observations requires to have PRMv2 implemented in a host atmospheric model, and to prepare for such an implementation the next section introduces a gridded product of InjH based upon PRMv2.

## 6 Towards a wildfire injection height climatology

Here we present a first gridded product of plume InjH distribution, based on the PRMv2 model optimised in Sect. 5. Since PRMv2 has currently been optimized using North American fires from the MISR plume height database, we only consider North America here, as per Sect. 5.1.2 (latitude = 35–70° N, longitude = 40–170° W). Sofiev et al. (2013) already derived a global distribution of maximum smoke emission height using a different approach also based upon MODIS FRP observations and estimates of the fire energy triggering plume updraft (Sofiev et al., 2012). In that work, MODIS-derived emissions fires were gridded on a  $1^\circ \times 1^\circ \times 500\text{m}$  global mesh at a monthly temporal resolution, and to account for periods between MODIS overpasses methods were developed to estimate the FRP diurnal cycle and to fill (probably cloud-related) gaps between apparently missing observations (grid cells where no fire was seen in a month but which are neighboured by at least 3 other cells with fires). In our approach we wish

9851

to primarily test the spatial variability of the PRMv2 model output, so that only fires actually detected in Collection 5 MODIS Active Fire products are included, with no adjustment for the diurnal cycle or cloud cover/missing observations. We clustered the detected fire pixels, and for each derived AF-area and FRP, and then estimated the biomass burning rate ( $\text{kg s}^{-1}$ ) from the FRP using the biome-dependent conversion factors from the current version of the Global Fire Assimilation System (GFAS Kaiser et al., 2012). Finally, we estimated the InjH of each plume using the optimised PRMv2 model, and gridded the results at a  $1.0^\circ$  resolution and a 6 hourly temporal interval. Each fire is assumed to last for 6 h, and if it remains undetected by subsequent MODIS observations it is assumed to be extinguished. Multiple overpasses of the same fire event are removed from the dataset, and only the highest FRP within each 6 h time slot are kept. Two observed “fire clusters” are considered to represent the same fire if they are not on the same granule, and are within a horizontal distance of 1 km or less. Our approach also assumes that smoke from fires with a AF-area lower than 1 ha are trapped within the boundary layer, since we know that AF-area estimates from smaller fires show increased inaccuracy (see Appendix B and in particular Fig. 16). Furthermore, in this first approach, fires from all land cover types are included in the gridded data, although agricultural fires would require further analysis (see discussion in Sect. 4.2).

The seasonal maps of wildfire plume InjH resulting from use of PRMv2 with the MODIS active fire data are shown in Figs. 11 and 12. For each season, biomass burning rates for each 6 h time slot are integrated and injected at the height predicted by PRMv2. Hence, the fire-consumed “mass” can be seen as a tracer to which biomass burning emission factors (e.g. Andreae and Merlet, 2001) should be applied in order to derive the corresponding trace gas concentration at each atmospheric level. For each season of 2003, Figs. 11 and 12 show the horizontal distribution of the seasonally integrated InjH median (equal fire-consumed mass above and below), all single fire events with a modelled plume above 5 km, and the seasonal vertical distribution of consumed mass integrated along the longitude.

9852

The fire events used here are the same as those in Fig. 10, but InjH is now reported as altitude above sea level (a.s.l.). The main point indicated by these gridded data is the strong seasonal variability of landscape fire injection height, with a large InjH maxima in summer where the highest plumes can reach 10 km altitude between latitudes 5 of 45 to 60° N, though most still remain below 2 km. In total, 92% of plume events with maximum altitudes > 5 km occur during the summer months. During all other seasons, plumes remain consistently below 6 km, and the median injection heights show a similar pattern as do the occurrences of high plumes, which could indicate that in this type 10 of 1° gridded product injection into the free troposphere is dominated by the highest plumes. This is not always the case though, since for example close to Hudson Bay (Canada) the InjH median remains quite low (< 3 km) despite a large number of higher altitude plumes occurring in this area, and this is due to the occurrence of a larger number of fires with low plume heights, seen in the vertical distribution of burnt mass where a high peak (> 1 Tg) appears close to the ground around 55° N latitude. This 15 demonstrates that the definition of product representing “average InjH” on a grid like this is sensitive to the distribution of InjH at the sub-grid scale, suggesting the requirement to ultimately include compensation for “missing” periods of observations due to e.g. MODIS overpass gaps and cloud cover.

In the vertical distribution of fire-consumed mass for Summer 2003, a peak of burnt 20 mass is clearly visible near 60° latitude between 7 and 8 km. This corresponds to a single large fire event which occurred on the 17 August in Alberta (Canada) around (59.64° N, 112.70° W), and which was observed by MODIS 3 times between 19:05 and 20:55 UTC. This fire was already mentioned by Stocks et al. (2005), who estimated that the plume reached the stratosphere. During this particular extreme fire event, the 25 fire front splits and spreads so quickly over the 110 min interval between the first and last MODIS observation of the 17th, that our simple method of “fire tracking” (detailed above in this section) fails. During the 6 h slot containing multiple MODIS observations of this particular event, the same fire were thus counted more than once. However, we are here mainly interested in the InjH estimate, and less so in the fire-consumed

9853

mass, so it is interesting to see that for this extreme fire the optimised PRMv2 model manages to simulate the occurrence of a very high altitude plume (6 to 8 km a.s.l.), though one that does not actually reach the stratosphere. Nevertheless, PRMv2 is the only approach of the four schemes tested that is able to predict this intense up-draft 5 (see Supplement for other model results over Summer 2003, Figs. S4–S6). Although this first evaluation of the spatial and seasonal variation in PRMv2-derived fire plume injection height does not constitute a true validation, it does demonstrate that even though our approach relies on the same dynamical core of the original Freitas et al. (2007) implementation (i.e. PRMv0), the en/de-trainment scheme we have added have 10 enhanced performance such that PRMv2 is more able to simulate the injection of high plumes rising up to 10 km.

## 7 Summary and conclusions

To improve the modelling of biomass burning (BB) emissions transport, several parametrizations of smoke plume injection height (InjH) for implementation in atmospheric chemical transport models have been proposed (Freitas et al., 2010; Rio et al., 2010; Sofiev et al., 2012), but due to the coupling of plume dynamics and ambient atmosphere their validation is difficult, in part because satellite EO data are currently unable to deliver simultaneous information on fire and plume evolution at time-scale of ~ 1 h or less and with a spatial resolution allowing the accurate derivation of sub-pixel fire information. 20

In this work, we therefore use a subset of the current North American MISR data of (Nelson et al., 2013), extracting fire events where plume and fire activity shows a relatively small change over consecutive Terra and Aqua MODIS observations. We identify a dataset of 38 “good” fires to optimize an improved version of the original 25 plume rise model (PRM) of Freitas et al. (2007), and extend the model to include (i) a new entrainment and detrainment scheme, (ii) a mass conservation equation, and (iii) a new method to estimate the convective energy released by the fire from a di-

9854

rect EO-observable (FRP). These developments of PRMv2 required introduction of six new parameters, whose values were estimated using a two fold optimization procedure based on Simulating Annealing and Markov chain Monte Carlo (McMC) uncertainty testing.

The limited number of fire events available did not allow us to properly validate PRMv2 using modelled vs observed height comparisons, but when applied to a year of MODIS active fire observations for North America PRMv2's response to the effect of atmospheric stability is consistent with previous findings showing a direct relationship between plume height and FRP for fire events in unstable atmospheres (Val Martin et al., 2010; Amiridis et al., 2010). In this first approach a simple model of 6 h fire persistence was used and we restraint our analysis to the year 2003 over North America. A comparison with other available parametrizations shows than PRMv2 is the model simulating the largest number of high plume ( $> 8\text{ km}$ ) and in the particular case of the year 2003 was the only model to capture a large fire event which occurs in Alberta (Canada).

After validation over more geographical locations (e.g. deforestation fire in South America), the application of PRMv2 to global fire inventory would be considered to set up "injection height climatology", which could be either used as a model validation dataset if transport models have a sub-grid fire plume model, or as climatological database to represent the effect of fire plumes in transport models (for models not having sub-grid parametrization).

From this work we conclude that plume rise models for application to landscape scale fires are still very much worth developing, since they may help us understand plume dynamics and in particular interpret the relatively sparse plume observations available from instruments such as MISR. However, as recommended by Val Martin et al. (2012) and Ichoku et al. (2012), a proper understanding and therefore correct parametrization of plume InjH will likely rely on high spatial and temporal resolution information, including ideally simultaneous field measurements of the key parameters driving smoke plume rise.

9855

## Appendix A: PRMv2 equations

### A1 Core equations

Using mass flux conservation, the Boussinesq approximation and introducing the variable  $\zeta = \rho R^2$  which can be read as the mass per altitude meter, mass conservation yields to

$$\partial_t \zeta = -\partial_z(w\zeta) + w\zeta(\epsilon - \delta) \quad (\text{A1})$$

where  $\epsilon$  and  $\delta [\text{m}^{-1}]$  are the entrainment and detrainment coefficients, respectively. They model the in- ( $u^+$ ) and out- ( $u^-$ ) coming horizontal flow in the plume as  $u^+ = \frac{Rw\epsilon}{2}$  and  $u^- = \frac{R\delta w}{2}$ . Extending to a scalar with a mixing ration  $\phi$ , the scalar transport equation is

$$\partial_t \zeta_{\text{sc}} = -\partial_z(w\zeta_{\text{sc}}) + w\zeta_{\text{sc}}(\epsilon - \delta) \quad (\text{A2})$$

where  $\zeta_{\text{sc}} = \rho\phi R^2$ . Assuming entrainment is controlled by ambient condition (Gregory, 2001), i.e.  $w\zeta_{\text{sc}}\epsilon = \rho R^2 w\epsilon\phi_e$ , with  $\phi_e$  the mixing ratio of the ambient scalar, the scalar conservation equation becomes

$$\partial_t \phi + w\partial_z \phi = -\epsilon w(\phi - \phi_e) \quad (\text{A3})$$

The vertical momentum equation is derived as in Simpson and Wiggert (1969) and Gregory (2001). The non hydrostatic pressure perturbation and the sub-grid turbulent flux are expressed as a linear combination of the buoyancy and the entrainment terms, which yields to

$$\partial_t w + w\partial_z w = \frac{1}{1+\gamma} gB - \epsilon w^2, \quad (\text{A4})$$

where  $\gamma = 0.5$  is the virtual mass coefficient introduced by Simpson and Wiggert (1969) and  $B = \frac{T_v - T_{ve}}{T_{ve}} - \text{LWC}$  the buoyancy term with LWC the reduction of buoyancy due to

9856

the weight of suspended water (Simpson and Wiggert, 1969) and  $T_v$  the virtual temperature.

The energy conservation is ensured by the temperature equation, where source terms are: the dry adiabatic lapse rate, latent heat (see Freitas et al., 2007 for details of the microphysical scheme) and lateral mixing with the ambient atmosphere (parametrized as in the momentum equation):

$$\partial_t T + w \partial_z T = -w \frac{g}{c_p} - \epsilon w(T - T_e) + (\partial_t T)|_{\text{micro}}. \quad (\text{A5})$$

Finally, as in PRMv0, the amplitude of the horizontal flow  $u$  is also transported to account for the drag effect of the ambient horizontal wind. Assuming that only momentum transfer is affecting  $u$  advection, and following the derivation of Eq. (A3) it yields

$$\partial_t u + w \partial_z u = -\epsilon w(u - u_e), \quad (\text{A6})$$

where  $u_e$  is the ambient atmospheric horizontal wind amplitude.

## A2 The en/de-trainment scheme

In PRMv2, the entrainment ( $\epsilon$ ) and detrainment ( $\delta$ ) coefficients are defined to account for the effect of the plume up-draft and the ambient wind shear.

The effect of vertical plume transport on horizontal flow is modelled following the work of Pergaud et al. (2009) on shallow convection parametrization. In a dry environment, on the basis of dimensional analysis, Pergaud et al. (2009) show that  $\epsilon_{\text{dry}}$  and  $\delta_{\text{dry}}$  are functions of both buoyancy and vertical velocity,

$$\epsilon_{\text{dry}}, \delta_{\text{dry}} \propto \frac{B}{w^2}.$$

Using coefficient factors based on LES simulations, Pergaud et al. (2009) define  $\epsilon_{\text{dry}}$  and  $\delta_{\text{dry}}$  as

$$\epsilon_{\text{dry}} = \max \left( 0, C_\epsilon \frac{B}{w^2} \right) \quad (\text{A7})$$

9857

$$\delta_{\text{dry}} = \max \left( \frac{1}{L_{\text{up}} - z}, C_\delta \frac{B}{w^2} \right) \quad (\text{A8})$$

with,  $C_\epsilon = 0.55$ ,  $C_\delta = -10$ .  $L_{\text{up}}$  is the Bougeault upward mixing length. It is a function of the turbulent kinetic energy (TKE) profile in the column, and is used here to ensure that the detrainment is not null in the mixing layer. In our case, the plume updraft is generally at its maximum in the PBL, and thus has positive buoyancy. To simplify the en/detrainment scheme, in our approach no detrainment induced by the plume updraft is applied in the mixing layer. When the plume reaches the lifting condensation level, Pergaud et al. (2009) switches the parametrization of the above lateral exchange to the model of Kain and Fritsch (1990). In the current state of development of PRMv2, the Kain and Fritsch (1990) scheme is not implemented yet.

The main difference between our approach to en/de-trainment, and that of Freitas et al. (2007), is that now the en/de-trainment scheme is no longer dependent of the plume radius  $R$ . In PRMv0, the entrainment coefficient is defined as  $\epsilon = 2\alpha R^{-1}$ , and  $R$  is derived following Turner (1973). In our approach, the new en/de-trainment scheme and the conservation mass equation make  $R$  more dependent of the local dynamics ( $w$ , buoyancy), which helps to control mass exchange and therefore vertical transport. However, in the case of fire plume the vertical updraft is expected to be much stronger than for shallow convection event. Therefore the constant parameters  $C_\epsilon$  and  $C_\delta$  need recalibration. Section 5 tackles this point. Note here that in shallow convection  $C_\epsilon$  is usually ranging from 0 to 1 (Gregory, 2001; Chikira and Sugiyama, 2010), as it is assumed that entrainment only acts again buoyancy which is the main source of momentum. As explained by Chikira and Sugiyama (2010), in their formalism if  $C_\epsilon = 1$ , it means that all the buoyancy used to accelerate the up-draft is balanced by the entrainment. In the case of a fire plume the buoyancy is no more the only source of momentum, indeed the heat released by the fire can triggers high velocity at ground level (see  $w_0$  in Eq. 8). Therefore we decide in our approach to relax the constraint on  $C_\epsilon$  and accept value grater than 1.

9858

To account also for wind shear effects in PRMv2, the approach of Freitas et al. (2010) is used. Based on dimensional analysis, the dynamical entrainment coefficient is defined as

$$\epsilon_{\text{dyn}} = C_{\epsilon,\text{dyn}} \frac{1}{w} \frac{du}{dz}.$$

- 5 This formulation shows that the stronger the updraft is, the less the plume is affected by wind shear (i.e. weak entrainment), and the stronger the wind shear the more likely the vertical propagation of the plume is stopped (i.e. strong entrainment). The dynamical detrainment  $\delta_{\text{dyn}}$ , which only affects the mass conservation equation (Eq. 3), is chosen to be directly proportional to  $\epsilon_{\text{dyn}}$ ,
- 10  $\delta_{\text{dyn}} = C_{\delta,\text{dyn}} \epsilon_{\text{dyn}}.$

This means that when the plume experiences the effect of wind shear, its dynamics will only be affected by  $\epsilon_{\text{dyn}}$ , while its mass gain/loss is controlled by the parameter  $C_{\delta,\text{dyn}}$ .

## Appendix B: Validation of the Dozier algorithm

### B1 Application of the Dozier algorithm to MODIS and BIRD HSRS radiance signal

- 15 To validate our implementation of the Dozier (1981) “dualband” approach to estimating fire effective temperature ( $T_f$ ) and sub-pixel active fire area (AF-area), along with the FRP estimate derived via these terms ( $\text{FRP}_{\text{doz}}$ ), we applied the Dozier (1981) algorithm to a series of wildfire events observed almost simultaneously by MODIS on the Terra satellite and by the Hotspot Recognition Sensor (HSRS) onboard the Bi-spectral Infrared Detection Experimental Small Satellite (BIRD), in a similar manner to the original BIRD-MODIS inter comparison study of (Wooster et al., 2003). HSRS

9859

- is specifically designed for making active fire retrievals using the Dozier (1981) “dualband” approach (Zhukov et al., 2006), and has a nadir ground pixel area roughly 10× smaller than MODIS and so should certainly provide more accurate active fire information than can be obtained from MODIS when both sensors view the same fire simultaneously (Wooster et al., 2003). From the BIRD archive, 38 fires were identified with time differences between them and the matching MODIS observation ranging from 20 to 84 min. The HSRS MIR band is located at  $\lambda_1 = 3.4\text{--}4.2\mu\text{m}$  and the TIR band at  $\lambda_2 = 8.5\text{--}9.3\mu\text{m}$ , similar to the MODIS band 21 ( $\lambda = 3.929\text{--}3.989\mu\text{m}$ , and band 29 ( $\lambda = 8.4\text{--}8.7\mu\text{m}$ ) that we use here as the MODIS inputs to the Dozier (1981) algorithm.
- 10 Observations from BIRD and MODIS of the same fire were geo-referenced to a geographic grid having a spacing similar to the double-sampling observation grid of the native HSRS raw data (185 m; Zhukov et al., 2006). Figure 13 provides an example of the output from this process.

- To make PRMv2 most easily applicable to the largest number of fire events seen with MODIS, we also applied the Dozier (1981) algorithm using MODIS band 31 ( $\lambda = 10.780\text{--}11.280\mu\text{m}$ ) instead of the band that most closely matches the LWIR of BIRD HSRS (MODIS Band 29), since along with the MIR band information, data from MODIS band 31 is included in the MODIS Collection 5 active fire product (i.e. the MOD14 product Justice et al., 2002). Using the MODIS band 21 and 31 data obviates the need to download and process the much larger level 1b MODIS data (i.e. the MOD021 km calibrated spectral radiance product), and our implementation of the Dozier (1981) algorithm can thus be run using the MOD14 files alone. Fire detection algorithms from Zhukov et al. (2006) and Giglio et al. (2003) are used to extract active fire pixels and calculate the spectral radiance signal of each fire cluster from the BIRD HSRS and MODIS data respectively. However, to estimate the background radiance, we explored an adaptation of existing methods since we noted that pixels nearby the fire cluster appear quite often to have lower brightness temperatures if they are overlain by thick smoke than if they are smoke free. Since such lowered brightness temperatures will affect the estimation of the “background signal” used as input to the Dozier algorithm

9860

(see Eq. 14), using the MOD021 km product we instead calculated the background radiance with the extremes removed from non-fire pixels selected within a  $5\text{ km} \times 5\text{ km}$  around the location of the fire cluster. Hereafter, a new mask (fire + valid background pixels, termed  $M_n$ ) is applied to both the BIRD and MODIS data. When using only the MOD14 product however,  $M_n$  cannot be calculated, since only the mean signal of the already identified background pixels is available in the MOD14 product file. In this case, fire pixel and background pixel radiances are respectively derived for each cluster as the sum of individual fire pixel radiances and the mean of their respective background radiances, as defined in Giglio et al. (2003). In the following description, this MOD14-derived mask is referred as  $M_{14}$ . The smoke contaminated pixels close to the fire are more likely to influence the background signal calculated using  $M_{14}$  than  $M_n$  not flagged cloud free and are likely to be part of the selected valid pixel of  $M_{14}$ . Thus, by using  $M_n$  we believe that we can lower the perturbing effect of the plume on background temperature estimation, and therefore improve the determination of the background radiance, in particular the TIR background radiance  $L_{b,2}$  which is an input whose uncertainties have a strong influence on the final Dozier retrievals (Giglio and Kendall, 2001; Wooster et al., 2003).

The Dozier algorithm is then applied to 5 different permutations of sensor ( $S = \text{BIRD}$  represented by Bi and MODIS represented by Mo), band ( $b = \text{MIR}, \text{TIR}$ ) and mask ( $M = M_n, M_{14}$ ). The 5 are  $[\text{Bi}^{\text{MIR}}, \text{Bi}^{\text{TIR}}]_{M_n^{\text{BIRD}}}$ ,  $[\text{Bi}^{\text{MIR}}, \text{Bi}^{\text{TIR}}]_{M_n}$ ,  $[\text{Mo}_{21}^{\text{MIR}}, \text{Mo}_{29}^{\text{TIR}}]_{M_n}$ ,  $[\text{Mo}_{21}^{\text{MIR}}, \text{Mo}_{31}^{\text{TIR}}]_{M_n}$ , and  $[\text{Mo}_{21}^{\text{MIR}}, \text{Mo}_{31}^{\text{TIR}}]_{M_{14}}$ .  $M_n^{\text{BIRD}}$  is using the new fire mask built on the output from the active fire detection algorithm of BIRD HSRS, while as described above  $M_n$  is based on the output from the MODIS active fire detection algorithm. However, since one MODIS active fire pixel can correspond to multiple BIRD active fire pixels, in the  $M_n^{\text{BIRD}}$  mask, the final active fire temperature and AF-area used for comparison with the matching MODIS observations are the mean temperature and the sum of the AF-area of the BIRD clusters present within the area covered by the MODIS fire mask (see Fig. 13).

9861

As a first test of our implementation, we compare the FRP retrieved via the outputs of the Dozier (1981) algorithm ( $\text{FRP}_{\text{doz}}$ ) to that calculated using the single band “MIR radiance” approach detailed in Wooster et al. (2003, 2005), here termed  $\text{FRP}_{\text{mir}}$ . A somewhat similar comparison just using BIRD HSRS data was previously shown by Wooster et al. (2003). Figure 14 shows the results of the comparison for the 5 different permutations introduced above. Results are only shown for the 24 fires of the 38 selected fire events observed near simultaneously by both BIRD and MODIS, since these are where the Dozier algorithm converges for every permutation. As discussed by Giglio and Kendall (2001), the Dozier (1981) algorithm does not always converge, and to do so requires (i) a cooling trail that does not exceed more than 50 times the active fire area, (ii) a reasonably strong fire thermal signature in both the MIR and TIR bands, which from MODIS means a fire larger than 0.3 ha, and (iii) an appropriately low uncertainty on the input data, particularly in the estimation of the TIR background radiance.

When using BIRD or MODIS data with the  $M_n$  mask,  $\text{FRP}_{\text{mir}}$  and  $\text{FRP}_{\text{doz}}$  match well ( $r^2 > 0.99$ ), meaning that the assumptions made in Eqs. (14)–(16) appear valid, in particular  $\epsilon_{f,i} = \epsilon_f = 1$  and  $(1 - p) \sim 1$ . Also note that the selection of the wavebands used does not greatly affect FRP derivation (see  $[\text{Mo}_{21}^{\text{MIR}}, \text{Mo}_{29}^{\text{TIR}}]_{M_n}$  and  $[\text{Mo}_{21}^{\text{MIR}}, \text{Mo}_{31}^{\text{TIR}}]_{M_n}$ ) and using  $M_n^{\text{BIRD}}$  or  $M_n$  affects essentially the low FRP of our fire selection. See difference between  $[\text{Bi}^{\text{MIR}}, \text{Bi}^{\text{TIR}}]_{M_n^{\text{BIRD}}}$  and  $[\text{Bi}^{\text{MIR}}, \text{Bi}^{\text{TIR}}]_{M_n}$ . This confirms that a higher spatial resolution sensor is more sensitive to lower amounts of fire activity than is a coarser spatial resolution sensor (Freeborn et al., 2009). Now, when considering the mask  $M_{14}$  Fig. 14 show a net degradation of the agreement between the FRPs. The only difference between  $[\text{Mo}_{21}^{\text{MIR}}, \text{Mo}_{31}^{\text{TIR}}]_{M_n}$ , and  $[\text{Mo}_{21}^{\text{MIR}}, \text{Mo}_{31}^{\text{TIR}}]_{M_{14}}$  comes from the derivation of the background radiance. Therefore the introduction of  $M_n$  seems to be effective in retrieving an appropriate background radiance.

To pursue the validation of our Dozier algorithm implementation, Figs. 15, 17 and 16 show a comparison between bands/mask selections for  $\text{FRP}_{\text{doz}}$ ,  $T_f$  and AF-area for the same 24 fires of Fig. 14.

9862

Assuming that  $(Bi^{MIR}, Bi^{TIR})_{M_n^{BIRD}}$  is the best available estimate of the fire sub-pixel characteristics (high spatial resolution, low noise, and wide dynamic range Giglio and Kendall, 2001; Zhukov et al., 2006), following the diagonal plots of Fig. 15 shows that lowering the BIRD spatial resolution ( $[Bi^{MIR}, Bi^{TIR}]_{M_n^{BIRD}}$  vs  $[Bi^{MIR}, Bi^{TIR}]_{M_n}$ ), swapping the sensor from BIRD to MODIS ( $[Bi^{MIR}, Bi^{TIR}]_{M_n}$  vs  $[Mo^{MIR}_{21}, Mo^{TIR}_{29}]_{M_n}$ ), changing the MODIS TIR waveband ( $[Mo^{MIR}_{21}, Mo^{TIR}_{29}]_{M_n}$  vs  $[Mo^{MIR}_{21}, Mo^{TIR}_{31}]_{M_n}$ ), and altering the active fire mask ( $[Mo^{MIR}_{21}, Mo^{TIR}_{31}]_{M_n}$  vs  $[Mo^{MIR}_{21}, Mo^{TIR}_{31}]_{M_{14}}$ ) all keep the retrieved  $FRP_{doz}$  within a factor 2. When considering the separate calculation of  $T_f$  (Fig. 17) and AF-area (Fig. 16), it appears that BIRD resolution decrease keeps AF-area within a factor 2 and  $T_f$  within  $\pm 100\text{K}$ . Sensor swap to MODIS keeps a fairly good correlation for  $T_f$ , but underestimates the active fire areas of small fires. Modification of the MODIS TIR band decreases  $T_f$  by  $\sim 25\%$ , and increases AF-area by a factor 2. This is consistent with (Giglio and Justice, 2003), since when using band 31 instead of 29, the TIR wavelength increases causes the system of equations to be more sensitive to lower temperatures and therefore to the cooling trail of the fire. Finally, using background temperatures directly from the MODIS collection 5 active product (i.e.  $M_{14}$ ) decreases the accuracy of the retrieval by another factor 2 for AF-area and adds a 100K error to  $T_f$ . Figures 15, 16 and 17 also show the time difference between the MODIS and BIRD overpasses, and indicate no consistent relationship between the magnitude of this time difference and the differences in retrieved fire characteristics coming from the two sensors. Finally, the upper left plots of Figs. 15, 17, and 16 show errors introduced when directly using data from the MOD14 product ( $[Mo^{MIR}_{21}, Mo^{TIR}_{31}]_{M_{14}}$ ) instead of the best available measure of BIRD ( $[Bi^{MIR}, Bi^{TIR}]_{M_n^{BIRD}}$ ). It appears that the error made on  $FRP_{doz}$  is acceptable, but AF-area is generally higher (sometime by more than a factor two) and  $T_f$  is underestimated by more than 100K for half of the fires. However, the trend remains seemingly correct, with a correlation on AF-area and  $T_f$  retrieval of around 0.7. This suggests that when applied to  $[Mo^{MIR}_{21}, Mo^{TIR}_{31}]_{M_{14}}$ , the Dozier algorithm is able to quantitatively differentiate between fires on the basis of their retrieved active fire area and temperature.

9863

titatively differentiate between fires on the basis of their retrieved active fire area and temperature.

## B2 Efficiency of the $\Delta_{11}$ test and the low sub-pixel temperature filter

Figure 18 shows the effect of the  $\Delta_{11}$  test of the TIR radiance signal introduced in Sect. 3.2, when applied to the system made of the low sub-pixel temperature filter (introduced in Sect. 3.2) and the Dozier (1981) algorithm. Using all available fires from the Northern American MISR data set, AF-area and fire temperature  $T_f$  are derived from the Dozier algorithm using the MOD14 data (above  $M_{14}$  mask) for the initial clusters (formed with the fire pixels present in the MOD14 product) and for the filtered clusters (clustered formed with only pixels having a sub-pixel temperature  $> 600\text{K}$ ).

When removing cool pixels, clusters should end up with higher active fire temperatures and smaller areas. Figure 18c shows that a threshold value of  $\Delta_{11} = 0.5 \text{ W m}^{-2} \text{ str}^{-1}$  gives therefore the optimal response of the filter. For values above  $\Delta_{11} = 0.5$ , the number of available clusters drops which decreases the statistical representativeness of the approach.

Figure 18a and 18b shows that applying the  $\Delta_{11}$  test removes initial small hot clusters ( $\text{AF-area} < 1\text{ ha}$  and  $T_f \gtrsim 900\text{K}$ ) where the Dozier algorithm fails to obtain higher temperatures and lower AF-area after application of the filter, see differences in  $T_f$  and AF-area between initial and filtered cluster for  $\Delta_{11} = 0$  (green) and 0.5 (red). The application of the TIR test leads to the conclusion that the Dozier algorithm is then more likely to converge when applied to large fires. Our approach suggests that for MODIS, a minimum fire size within a cluster of around 1ha is required for strong Dozier algorithm performance. This echo's the findings of Giglio and Kendall (2001), though our lower limit is somewhat reduced compared to their estimate.

In the scope of this study, we suggest that our implementation of the Dozier algorithm based on the MOD14 data is able to characterize fires clusters by their effective active fire temperature and area, and that when applied to flaming dominated clusters where the TIR band signal is well characterized from the background

9864

( $\Delta_{11} = L_2 - L_{b,2} > 0.5 \text{ W m}^{-2} \text{ str}^{-1}$ ), cluster active fire temperature and area show a consistent behaviour which supports the convergence of the algorithm. We also note that the retrieved active fire temperature and area are not directly physically interpretable as the true temperature and area of the fire activity, unlike the FRP which is interpretable as the overall radiative power of the fire, but that the active fire area parameter is able to be used within the optimised plume rise model (PRMv2) to characterise the area over which the fires radiant (and also convective) heat is released.

### Appendix C: Near infrared colour composite image

The colors in the NIR colour composite image shown in Fig. 6 can be explained as follows:

- Red – this represents a pixel containing an actively burning fire. The peak wavelength of spectral emittance of a landscape scale fire is within or close to the shortwave infrared (SWIR) spectral region. Therefore, a consequently increased 2.1  $\mu\text{m}$  signal causes the fire pixel to appear red in the colour composite, even when the fire is highly sub-pixel.
- White – this represents a pixel containing large particles: e.g. water droplets or ice particles. These scatter electromagnetic radiation at the wavelengths used to create the NIR colour composite approximately equally, due to their large size and resultant non-selective scattering. For this reason, the same pixels also appear white in the simulated true color composite.
- Blue/cyan for pixels in the plume, coupled with bright pixels in the simulated true color composite image: pixel containing more ice than water droplets, because reflectance of ice is lower than water at 2.1  $\mu\text{m}$ . A comparison with the optical phase detection algorithm of the MODIS cloud product shows a rather good match.

9865

- Blue – this represents pixels containing smaller scattering particles, since the 0.6  $\mu\text{m}$  wavelength radiation is being preferentially scattered by Rayleigh scattering.
- Black – this represents pixels where the land surface is either a lake, river or ocean, or is a recently burned area (water and the black ash typically laid down by fires has a low reflectance at IR wavelengths).
- Green – this represents a pixel containing substantial live vegetation, which has a high reflectance in the NIR spectral region.

**The Supplement related to this article is available online at  
doi:10.5194/acpd-15-9815-2015-supplement.**

**Acknowledgements.** Various components of this study were supported by the NERC grant NE/E016863/1, by the NERC National Centre for Earth Observation (NCEO), and also by the EU in the FP7 and H2020 projects MACC-II and MACC-III (contracts 283576 and 633080). The authors thank ECMWF for providing meteorological data, and the DLR BIRD Team and Zebris GMbh for providing the BIRD HSRS datasets used herein. NASA is acknowledged for the MODIS and MISR data used within this study, and the MISR Plume Height Project using the MINX tool is acknowledged for its provision of the plume height and other information used.

### References

- Amiridis, V., Giannakaki, E., Balis, D. S., Gerasopoulos, E., Pytharoulis, I., Zanis, P., Kazadzis, S., Melas, D., and Zerefos, C.: Smoke injection heights from agricultural burning in Eastern Europe as seen by CALIPSO, *Atmos. Chem. Phys.*, 10, 11567–11576, doi:10.5194/acp-10-11567-2010, 2010. 9841, 9850, 9855
- Andreae, M. O. and Merlet, P.: Emission of trace gases and aerosols from biomass burning, *Global Biogeochem. Cy.*, 15, 955–966, doi:10.1029/2000GB001382, 2001. 9852

9866

- Berk, A., Anderson, G. P., Acharya, P. K., Bernstein, L. S., Muratov, L., Lee, J., Fox, M., Adler-Golden, S. M., Chetwynd, Jr., J. H., Hoke, M. L., Lockwood, R. B., Gardner, J. A., Cooley, T. W., Borel, C. C., Lewis, P. E., and Shettle, E. P.: MODTRAN5: 2006 update, Proc. SPIE, 6233, 62331F–62331F–8, doi:10.1117/12.665077, 2006. 9829
- Braswell, B. H., Sacks, W. J., Linder, E., and Schimel, D. S.: Estimating diurnal to annual ecosystem parameters by synthesis of a carbon flux model with eddy covariance net ecosystem exchange observations, *Glob. Change Biol.*, 11, 335–355, 2005. 9843, 9846
- Chen, Y., Li, Q., Randerson, J. T., Lyons, E. A., Kahn, R. A., Nelson, D. L., and Diner, D. J.: The sensitivity of CO and aerosol transport to the temporal and vertical distribution of North American boreal fire emissions, *Atmos. Chem. Phys.*, 9, 6559–6580, doi:10.5194/acp-9-6559-2009, 2009. 9818, 9819, 9820
- Chikira, M. and Sugiyama, M.: A cumulus parameterization with state-dependent entrainment rate. Part I: Description and sensitivity to temperature and humidity profiles, *J. Atmos. Sci.*, 67, 2171–2193, doi:10.1175/2010jas3316.1, 2010. 9847, 9858
- Colarco, P. R., Schoeberl, M. R., Doddridge, B. G., Marufu, L. T., Torres, O., and Welton, E. J.: Transport of smoke from Canadian forest fires to the surface near Washington, D.C.: injection height, entrainment, and optical properties, *J. Geophys. Res.-Atmos.*, 109, D06203, doi:10.1029/2003JD004248, 2004. 9819
- Dirksen, R. J., Folkert Boersma, K., de Laat, J., Stammes, P., van der Werf, G. R., Val Martin, M., and Kelder, H. M.: An aerosol boomerang: rapid around-the-world transport of smoke from the December 2006 Australian forest fires observed from space, *J. Geophys. Res.-Atmos.*, 114, D21201, doi:10.1029/2009JD012360, 2009. 9819
- Dozier, J.: A method for satellite identification of surface temperature fields of subpixel resolution, *Remote Sens. Environ.*, 11, 221–229, doi:10.1016/0034-4257(81)90021-3, 1981. 9821, 9825, 9829, 9830, 9831, 9832, 9842, 9850, 9859, 9860, 9862, 9864, 9881, 9891, 9892, 9893, 9894
- ECMWF: IFS documentation Part IV: Physical Processes, Tech. Rep. CY38r1, European Center for Medium-Range Weather Forecasts, Shinfield Park, Reading, UK, available at: <http://old.ecmwf.int/research/ifsdocs/CY38r1/IFSPart4.pdf> (last access: March 2015), 2012. 9836
- Elguindi, N., Clark, H., Ordóñez, C., Thouret, V., Flemming, J., Stein, O., Huijnen, V., Moinat, P., Inness, A., Peuch, V.-H., Stohl, A., Turquety, S., Athier, G., Cammas, J.-P., and Schultz, M.: Current status of the ability of the GEMS/MACC models to reproduce the tropo-

9867

- spheric CO vertical distribution as measured by MOZAIC, *Geosci. Model Dev.*, 3, 501–518, doi:10.5194/gmd-3-501-2010, 2010. 9819
- Freeborn, P., Wooster, M., Roberts, G., Malamud, B., and Xu, W.: Development of a virtual active fire product for Africa through a synthesis of geostationary and polar orbiting satellite data, *Remote Sens. Environ.*, 113, 1700–1711, doi:10.1016/j.rse.2009.03.013, 2009. 9862
- Freeborn, P. H., Wooster, M. J., Hao, W. M., Ryan, C. A., Nordgren, B. L., Baker, S. P., and Ichoku, C.: Relationships between energy release, fuel mass loss, and trace gas and aerosol emissions during laboratory biomass fires, *J. Geophys. Res.-Atmos.*, 113, D01301, doi:10.1029/2007JD008679, 2008. 9827
- Freitas, S. R., Longo, K. M., Chatfield, R., Latham, D., Silva Dias, M. A. F., Andreae, M. O., Prins, E., Santos, J. C., Gielow, R., and Carvalho Jr., J. A.: Including the sub-grid scale plume rise of vegetation fires in low resolution atmospheric transport models, *Atmos. Chem. Phys.*, 7, 3385–3398, doi:10.5194/acp-7-3385-2007, 2007. 9819, 9821, 9822, 9823, 9824, 9826, 9827, 9854, 9857, 9858
- Freitas, S. R., Longo, K. M., Trentmann, J., and Latham, D.: Technical Note: Sensitivity of 1-D smoke plume rise models to the inclusion of environmental wind drag, *Atmos. Chem. Phys. Discuss.*, 9, 14713–14733, doi:10.5194/acpd-9-14713-2009, 2009. 9820, 9821, 9823, 9824, 9854, 9859
- Fromm, M., Lindsey, D. T., Servranckx, R., Yue, G., Trickl, T., Sica, R., Doucet, P., and Godin-Beekmann, S.: The untold story of pyrocumulonimbus, *B. Am. Meteorol. Soc.*, 91, 1193–1209, doi:10.1175/2010BAMS3004.1, 2010. 9820, 9851
- Fromm, M. D. and Servranckx, R.: Transport of forest fire smoke above the tropopause by supercell convection, *Geophys. Res. Lett.*, 30, 1542, doi:10.1029/2002GL016820, 2003. 9818
- Gelman, A., Carlin, J. B., Stern, H. S., and Rubin, D. B.: *Markov Chain Simulation*, chap. 11, Chapman and Hall/CRC, New York, 2000. 9845
- Giglio, L. and Justice, C. O.: Effect of wavelength selection on characterization of fire size and temperature, *Int. J. Remote Sens.*, 24, 3515–3520, doi:10.1080/0143116031000117056, 2003. 9824, 9863
- Giglio, L. and Kendall, J. D.: Application of the Dozier retrieval to wildfire characterization: a sensitivity analysis, *Remote Sens. Environ.*, 77, 34–49, doi:10.1016/S0034-4257(01)00192-4, 2001. 9830, 9861, 9862, 9863, 9864

9868

- Giglio, L. and Schroeder, W.: A global feasibility assessment of the bi-spectral fire temperature and area retrieval using {MODIS} data, *Remote Sens. Environ.*, 152, 166–173, doi:10.1016/j.rse.2014.06.010, 2014. 9824, 9830, 9831
- Giglio, L., Descloitres, J., Justice, C. O., and Kaufman, Y. J.: An enhanced contextual fire detection algorithm for {MODIS}, *Remote Sens. Environ.*, 87, 273–282, doi:10.1016/S0034-4257(03)00184-6, 2003. 9850, 9860, 9861, 9881, 9887, 9890, 9895
- Giglio, L., Randerson, J. T., van der Werf, G. R., Kasibhatla, P. S., Collatz, G. J., Morton, D. C., and DeFries, R. S.: Assessing variability and long-term trends in burned area by merging multiple satellite fire products, *Biogeosciences*, 7, 1171–1186, doi:10.5194/bg-7-1171-2010, 2010. 9817
- Gonzi, S. and Palmer, P. I.: Vertical transport of surface fire emissions observed from space, *J. Geophys. Res.-Atmos.*, 115, D02306, doi:10.1029/2009JD012053, 2010. 9818
- Goodrick, S. L., Achtemeier, G. L., Larkin, N. K., Liu, Y., and Strand, T. M.: Modelling smoke transport from wildland fires: a review, *Int. J. Wildland Fire*, 22, 83–94, doi:10.1071/WF11116, 2013. 9820
- Gregory, D.: Estimation of entrainment rate in simple models of convective clouds, *Q. J. Roy. Meteor. Soc.*, 127, 53–72, doi:10.1002/qj.49712757104, 2001. 9826, 9847, 9856, 9858
- Ichoku, C. and Ellison, L.: Global top-down smoke-aerosol emissions estimation using satellite fire radiative power measurements, *Atmos. Chem. Phys.*, 14, 6643–6667, doi:10.5194/acp-14-6643-2014, 2014. 9818
- Ichoku, C., Kahn, R., and Chin, M.: Satellite contributions to the quantitative characterization of biomass burning for climate modeling, *Atmos. Res.*, 111, 1–28, doi:10.1016/j.atmosres.2012.03.007, 2012. 9855
- Johnston, J. M., Wooster, M. J., and Lynham, T. J.: Experimental confirmation of the MWIR and LWIR grey body assumption for vegetation fire flame emissivity, *Int. J. Wildland Fire*, 23, 463–479, doi:10.1071/WF12197, 2014. 9827
- Justice, C., Giglio, L., Korontzi, S., Owens, J., Morisette, J., Roy, D., Descloitres, J., Alleaume, S., Petitcolin, F., and Kaufman, Y.: The Moderate Resolution Imaging Spectroradiometer (MODIS): a new generation of Land Surface Monitoring, *Remote Sens. Environ.*, 83, 244–262, doi:10.1016/S0034-4257(02)00076-7, 2002. 9824, 9834, 9860
- Kahn, R. A., Li, W.-H., Moroney, C., Diner, D. J., Martonchik, J. V., and Fishbein, E.: Aerosol source plume physical characteristics from space-based multiangle imaging, *J. Geophys. Res.-Atmos.*, 112, D11205, doi:10.1029/2006JD007647, 2007. 9820, 9825, 9839

9869

- Kahn, R. A., Chen, Y., Nelson, D. L., Leung, F.-Y., Li, Q., Diner, D. J., and Logan, J. A.: Wildfire smoke injection heights: two perspectives from space, *Geophys. Res. Lett.*, 35, L04809, doi:10.1029/2007GL032165, 2008. 9819
- Kain, J. S. and Fritsch, J. M.: A one-dimensional entraining/detraining plume model and its application in convective parameterization, *J. Atmos. Sci.*, 47, 2784–2802, 1990. 9858
- Kaiser, J. W., Heil, A., Andreae, M. O., Benedetti, A., Chubarova, N., Jones, L., Morcrette, J.-J., Razinger, M., Schultz, M. G., Suttie, M., and van der Werf, G. R.: Biomass burning emissions estimated with a global fire assimilation system based on observed fire radiative power, *Biogeosciences*, 9, 527–554, doi:10.5194/bg-9-527-2012, 2012. 9818, 9852
- Kirkpatrick, S., Gelatt, C. D., and Vecchi, M. P.: Optimization by simulated annealing, *Science*, 220, 671–680, doi:10.1126/science.220.4598.671, 1983. 9843
- Latham, D.: PLUMP: A one-dimensional plume predictor and cloud model for fire and smoke managers, General Technical Report INT-GTR-314, Intermountain Research Station, USDA Forest Service, November, 1994. 9821, 9823
- Lavoué, D., Lioussse, C., Cachier, H., Stocks, B. J., and Goldammer, J. G.: Modeling of carbonaceous particles emitted by boreal and temperate wildfires at northern latitudes, *J. Geophys. Res.-Atmos.*, 105, 26871–26890, doi:10.1029/2000JD900180, 2000. 9841
- Liu, Y., Achtemeier, G. L., Goodrick, S. L., and Jackson, W. A.: Important parameters for smoke plume rise simulation with Daysmoke, *Atmospheric Pollution Research*, 1, 250–259, doi:10.5094/APR.2010.032, 2010. 9820
- McCarter, R. J. and Broido, A.: Radiative and convective energy from wood crib fires, *Pyro-dynamics*, 2, 65–85, 1965. 9823, 9827
- Metropolis, N., Rosenbluth, A. W., Rosenbluth, M. N., Teller, A. H., and Teller, E.: Equation of state calculations by fast computing machines, *J. Chem. Phys.*, 21, 1087–1092, doi:10.1063/1.1699114, 1953. 9843
- Morton, B. R., Taylor, G., and Turner, J. S.: Turbulent gravitational convection from maintained and instantaneous sources, *P. Roy. Soc. Lond. A Mat.*, 234, 1–23, 1956. 9827
- Nelson, D. L., Garay, M. J., Kahn, R. A., and Dunst, B. A.: Stereoscopic height and wind retrievals for aerosol plumes with the MISR INteractive eXplorer (MINX), *Remote Sens.*, 5, 4593–4628, doi:10.3390/rs5094593, 2013. 9819, 9829, 9833, 9834, 9838, 9854, 9877, 9878, 9879, 9881, 9883
- Paugam, R., Wooster, M., Freitas, S. R., and Val Martin, M.: A review of approaches to estimate wildfire plume injection height within large scale atmospheric chemical transport mod-

9870

- els – Part 1, *Atmos. Chem. Phys. Discuss.*, 15, 9767–9813, doi:10.5194/acpd-15-9767-2015, 2015. 9819, 9820, 9821, 9823, 9824, 9837, 9839
- Pergaud, J., Masson, V., Malardel, S., and Couvreux, F.: A parameterization of dry thermals and shallow cumuli for mesoscale numerical weather prediction, *Bound.-Lay. Meteorol.*, 132, 83–106, 2009. 9826, 9847, 9857, 9858
- Peterson, D., Wang, J., Ichoku, C., Hyer, E., and Ambrosia, V.: A sub-pixel-based calculation of fire radiative power from {MODIS} observations: 1: Algorithm development and initial assessment, *Remote Sens. Environ.*, 129, 262–279, doi:10.1016/j.rse.2012.10.036, 2013. 9831, 9833
- Peterson, D., Hyer, E., and Wang, J.: Quantifying the potential for high-altitude smoke injection in the North American boreal forest using the standard MODIS fire products and subpixel-based methods, *J. Geophys. Res.-Atmos.*, 119, 3401–3419, doi:10.1002/2013JD021067, 2014. 9832, 9842, 9883
- Prins, E. M., Feltz, J. M., Menzel, W. P., and Ward, D. E.: An overview of GOES-8 diurnal fire and smoke results for SCAR-B and 1995 fire season in South America, *J. Geophys. Res.-Atmos.*, 103, 31821–31835, doi:10.1029/98JD01720, 1998. 9823, 9830
- Reutter, P., Trentmann, J., Seifert, A., Neis, P., Su, H., Chang, D., Herzog, M., Wernli, H., Andreae, M. O., and Pöschl, U.: 3-D model simulations of dynamical and microphysical interactions in pyroconvective clouds under idealized conditions, *Atmos. Chem. Phys.*, 14, 7573–7583, doi:10.5194/acp-14-7573-2014, 2014. 9820
- Rio, C., Hourdin, F., and Chédin, A.: Numerical simulation of tropospheric injection of biomass burning products by pyro-thermal plumes, *Atmos. Chem. Phys.*, 10, 3463–3478, doi:10.5194/acp-10-3463-2010, 2010. 9821, 9854
- Roberts, G., Wooster, M. J., and Lagoudakis, E.: Annual and diurnal african biomass burning temporal dynamics, *Biogeosciences*, 6, 849–866, doi:10.5194/bg-6-849-2009, 2009. 9839
- Shephard, M. and Kennelly, E.: Effect of band-to-band coregistration on fire property retrievals, *IEEE T. Geosci. Remote*, 41, 2648–2661, doi:10.1109/tgrs.2003.814912, 2003. 9831
- Simpson, J. and Wiggert, V.: Models of precipitating cumulus towers, *Mon. Weather Rev.*, 97, 471–489, 1969. 9826, 9856, 9857
- Smith, A., Wooster, M., Drake, N., Perry, G., Dipotso, F., Falkowski, M., and Hudak, A. T.: Testing the potential of multi-spectral remote sensing for retrospectively estimating fire severity in African savanna environments, *Remote Sens. Environ.*, 97, 92–115, 2005. 9817

9871

- Smith, W. L. and Platt, C. M. R.: Comparison of satellite-deduced cloud heights with indications from radiosonde and ground-based laser measurements, *J. Appl. Meteorol.*, 17, 1796–1802, doi:10.1175/1520-0450(1978)017<1796:COSDCH>2.0.CO;2, 1978. 9841
- Sofiev, M., Ermakova, T., and Vankevich, R.: Evaluation of the smoke-injection height from wildland fires using remote-sensing data, *Atmos. Chem. Phys.*, 12, 1995–2006, doi:10.5194/acp-12-1995-2012, 2012. 9821, 9834, 9835, 9850, 9851, 9854, 9887
- Sofiev, M., Vankevich, R., Ermakova, T., and Hakkarainen, J.: Global mapping of maximum emission heights and resulting vertical profiles of wildfire emissions, *Atmos. Chem. Phys.*, 13, 7039–7052, doi:10.5194/acp-13-7039-2013, 2013. 9851
- Stocks, B. J., Fromm, M., Servranckx, R., Miller, S., Turk, J., and Diner, D.: Smoking Pyrocumulonimbus: analysis of a major Canadian boreal fire blowup from satellite and ground measurements, in: American Geophysical Union, Fall Meeting, abstract A31C-07, 2005. 9853
- Trentmann, J., Luderer, G., Winterrath, T., Fromm, M. D., Servranckx, R., Textor, C., Herzog, M., Graf, H.-F., and Andreae, M. O.: Modeling of biomass smoke injection into the lower stratosphere by a large forest fire (Part I): reference simulation, *Atmos. Chem. Phys.*, 6, 5247–5260, doi:10.5194/acp-6-5247-2006, 2006. 9839
- Turner, J. S.: *Buoyancy Effects in Fluids*, Cambridge University Press, Cambridge, doi:10.1017/CBO9780511608827, Cambridge Books Online, 1973. 9858
- Turquety, S., Logan, J. A., Jacob, D. J., Hudman, R. C., Leung, F. Y., Heald, C. L., Yantosca, R. M., Wu, S., Emmons, L. K., Edwards, D. P., and Sachse, G. W.: Inventory of boreal fire emissions for North America in 2004: importance of peat burning and pyroconvective injection, *J. Geophys. Res.-Atmos.*, 112, D12S03, doi:10.1029/2006JD007281, 2007. 9818
- Val Martin, M., Logan, J. A., Kahn, R. A., Leung, F.-Y., Nelson, D. L., and Diner, D. J.: Smoke injection heights from fires in North America: analysis of 5 years of satellite observations, *Atmos. Chem. Phys.*, 10, 1491–1510, doi:10.5194/acp-10-1491-2010, 2010. 9819, 9834, 9841, 9842, 9850, 9855, 9883
- Val Martin, M., Kahn, R. A., Logan, J. A., Paugam, R., Wooster, M., and Ichoku, C.: Space-based observational constraints for 1-D fire smoke plume-rise models, *J. Geophys. Res.-Atmos.*, 117, D22204, doi:10.1029/2012JD018370, 2012. 9819, 9821, 9822, 9824, 9825, 9834, 9835, 9855
- van der Werf, G. R., Randerson, J. T., Giglio, L., Collatz, G. J., Mu, M., Kasibhatla, P. S., Morton, D. C., DeFries, R. S., Jin, Y., and van Leeuwen, T. T.: Global fire emissions and the

9872

- contribution of deforestation, savanna, forest, agricultural, and peat fires (1997–2009), *Atmos. Chem. Phys.*, 10, 11707–11735, doi:10.5194/acp-10-11707-2010, 2010. 9818
- Ward, D. S., Kloster, S., Mahowald, N. M., Rogers, B. M., Randerson, J. T., and Hess, P. G.: The changing radiative forcing of fires: global model estimates for past, present and future, *Atmos. Chem. Phys.*, 12, 10857–10886, doi:10.5194/acp-12-10857-2012, 2012. 9818
- Wooster, M. J., Zhukov, B., and D., O.: Fire radiative energy for quantitative study of biomass burning: derivation from the BIRD experimental satellite and comparison to MODIS fire products, *Remote Sens. Environ.*, 86, 83–107, 2003. 9830, 9831, 9832, 9859, 9860, 9861, 9862
- Wooster, M. J., Roberts, G., Perry, G. L. W., and Kaufman, Y. J.: Retrieval of biomass combustion rates and totals from fire radiative power observations: FRP derivation and calibration relationships between biomass consumption and fire radiative energy release, *J. Geophys. Res.-Atmos.*, 110, D24311, doi:10.1029/2005JD006318, 2005. 9830, 9832, 9862, 9891
- Xu, W., Wooster, M., Roberts, G., and Freeborn, P.: New GOES imager algorithms for cloud and active fire detection and fire radiative power assessment across North, South and Central America, *Remote Sens. Environ.*, 114, 1876–1895, doi:10.1016/j.rse.2010.03.012, 2010. 9824
- Zhukov, B., Lorenz, E., Oertel, D., Wooster, M., and Roberts, G.: Spaceborne detection and characterization of fires during the bi-spectral infrared detection (BIRD) experimental small satellite mission (2001–2004), *Remote Sens. Environ.*, 100, 29–51, doi:10.1016/j.rse.2005.09.019, 2006. 9830, 9831, 9860, 9863, 9890

9873

**Table 1.** Input parameters of the PRMv2 model. See Sect. 2.2 for a description of each parameters. Parameter values calculated from the Simulated Annealing (SA) algorithm ( $d_{\text{SA}}$ ) and the 68% confidence interval estimated from the Markov chain Monte Carlo (McMC) algorithm ( $d_{\text{McMC}}$ ) and the set of input parameters finally selected ( $d_{\text{opt}}$ ) are reported.

Parameter	used in / Eqs.	range	$d_{\text{SA}}$	$d_{\text{McMC}}$	68 % CI	$d_{\text{opt}}$
$\alpha$	$w_0$ / (8) and (9)	[0.001, 0.1]	0.04	0.02, 0.07	0.039	
$C_e$	$\epsilon$ / (A7)	[0.01, 5]	2.27	1.6, 2.8	1.98	
$C_\delta$	$\delta$ / (A8)	[-25, -8]	-8.00	-19.1, -8.4	-9.78	
$C_{e,\text{dyn}}$	$\epsilon$ / (A7)	[0.3, 5]	1.99	1.1, 4.2	1.88	
$C_{\delta,\text{dyn}}$	$\delta$ / (A8)	[3, 40]	16.7	3.8, 20.4	8.37	
$\beta$	CHF / (10)	[0.5, 20]	1.00	0.2, 2.2	0.88	

9874

**Table 2.** Number of high fire plumes predicted by the 4 different plume rise models when run on all Northern American fires of 2003 detected by the Moderate-resolution Imaging Spectroradiometer (MODIS) and reported in the collection 5 of the active fire product. Same fires are used in Fig. 10. Height is Above Ground Level and in kilometres.

model	number of plume > 4 km	number of plume > 6 km	number of plume > 8 km	maximum plume height (km)
Sofiev	51	1	0	7.09
PRMv0	12	2	2	8.55
PRMv1	18	3	2	9.15
PRMv2	278	64	14	9.65

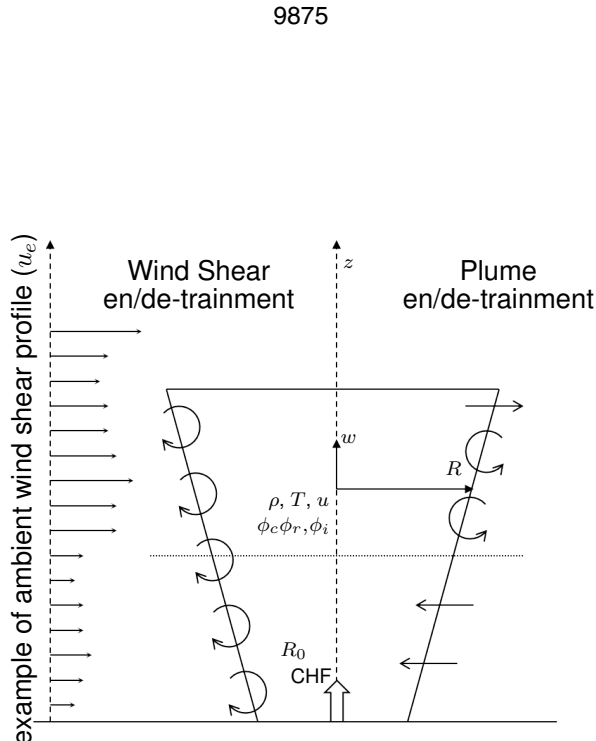


**Figure 1.** Sketch of fire plume dynamics as parametrized in the PRMv2 plume rise model developed herein.  $z$  is the vertical dimension, and the prognostic variables of the model are the vertical wind speed  $w(z)$ , the horizontal plume velocity  $u(z)$ , the quantity  $\zeta = \rho R^2$  with  $\rho(z)$  the air density in the plume and  $R(z)$  the plume radius, the air temperature in the plume  $T(z)$  and the mixing ratio of cloud, rain and ice ( $\phi_c$ ,  $\phi_r$  and  $\phi_i$ ). Boundary conditions are the convective heat flux (CHF) and active fire area (AF-area) (see Sect. 4 for more details on CHF and AF-area derivation). The horizontal flow is fully parametrized (only amplitude matters) to solve en-de/trainment effects from wind shear and plume up-draft (since the 1-D-model does not have a horizontal dimension, the left and right sides of the figure are not properly representative of its operation). See Appendix A for more details on the derivation of the PRMv2 equations.

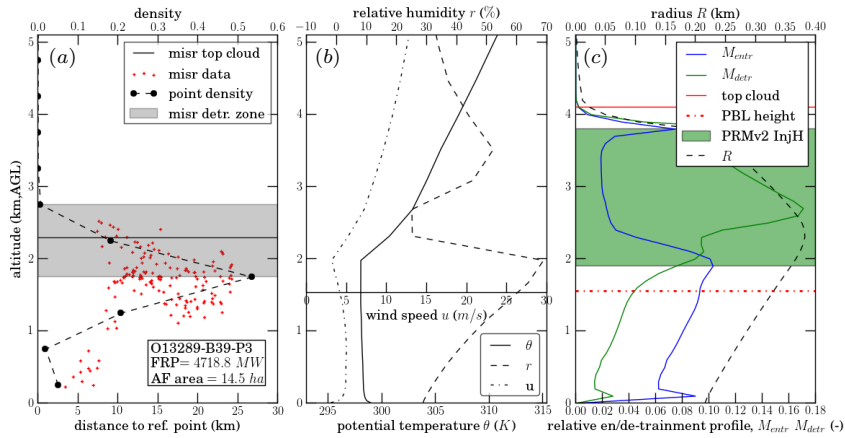


**Figure 2.** Example of the input and output of the PRMv2 model for the fire O13289-B39-P3 of the MISR plume height dataset (Nelson et al., 2013), with input parameters defined as in Sect. 5. The raw MISR measurement of the plume top height at each pixel, the density distribution of pixel height in the plume stack (see Sect. 4.1), the derived MISR detrainment zone (see Sect. 4.1), and the input data for PRMv2 (FRP, AF-area, and ambient atmospheric profile) are reported in panels (a) and (b). Panel (c) shows the PRMv2 output, where  $M_{\text{entr}}$  and  $M_{\text{detr}}$  are the relative entrainment and detrainment profile as defined in Eqs. (11) and (12), “PBL height” is the height of the planetary boundary layer obtained from the European Centre for Medium-range Weather Forecasts diagnostic,  $R$  is the radius of the plume, and “PRMv2 InjH” is the InjH simulated with PRMv2 as defined in Sect. 2.2.

9877

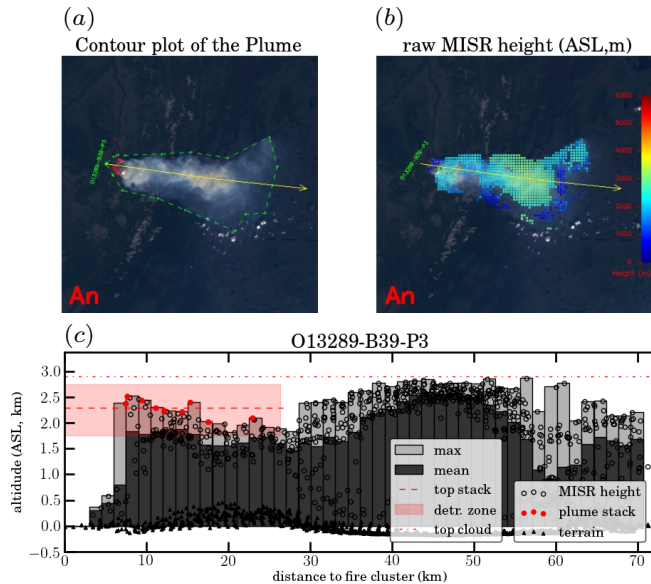


**Figure 3.** Methodology used here to derive injection height estimate from MISR plume top height observations, as applied to the fire O13289-B39-P3 of the MISR-derived plume height data set of Nelson et al. (2013). (a) shows the plume contour as defined in the MINX tool used to derive the MISR plume heights, superimposed on the MISR nadir view image, whilst (b) shows the raw MISR-derived plume height distribution. (c) Shows the distribution of MISR-derived plume height along the length of the plume transect shown in (a) and (b). This distribution is used to define the plume “stack” close to the fire, where transport is not yet dominated by the atmosphere (shown as the red rectangle). The plume injection height is then defined from the distribution of pixel heights seen within the “stack”.

9878

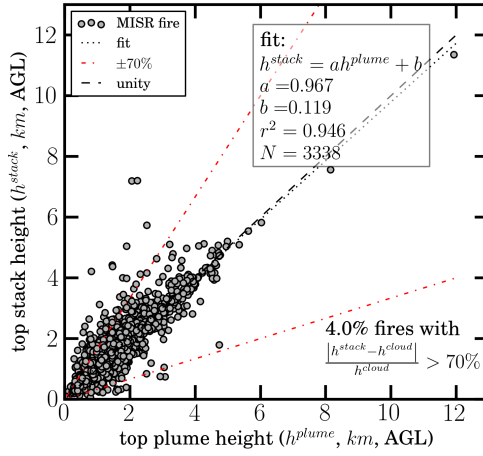


**Figure 4.** Comparison between the smoke plume injection height measured at the location of the plume stack ( $h^{\text{stack}}$ ) calculated using the MISR-based methodology presented in Fig. 3, and the plume top height  $h^{\text{plume}}$  as defined in the MISR plume height product (Nelson et al., 2013). The 4 % of fires having a difference of more than 70 % between this two metrics are removed from our training dataset, as detailed in Sect. 4.1. The black dashed line shows the 1-to-1 relationship between  $h^{\text{stack}}$  and  $h^{\text{plume}}$ . The red lines show the 70 % range of validity used herein, whilst the dotted black line shows the best fit between  $h^{\text{stack}}$  and  $h^{\text{plume}}$  for the final set of “valid” plume.

9879

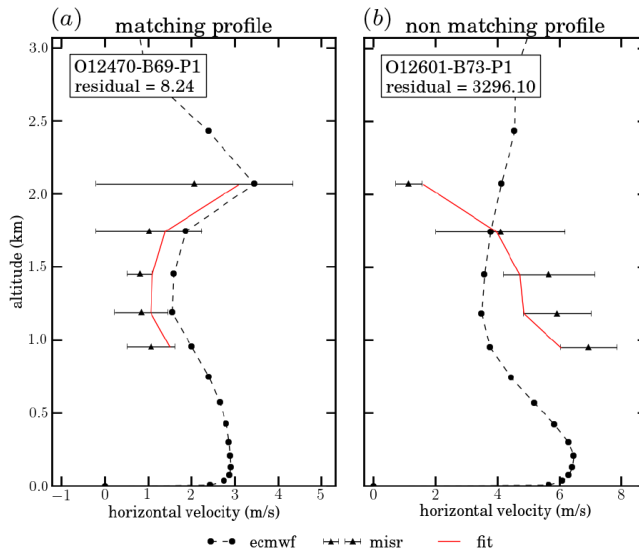


**Figure 5.** Example of horizontal wind amplitude profile at a fire location, as extracted from the ECMWF analysis (black dashed line) and as derived from the MISR plume height product (triangular points). The red line shows the best fit that minimizes the residual error defined by Eq. (17). **(a)** shows a correct match where the plume is selected for further analysis, whereas **(b)** shows a plot where the ECMWF and MISR-derived wind fields disagree significantly and which is removed from the training dataset.

9880

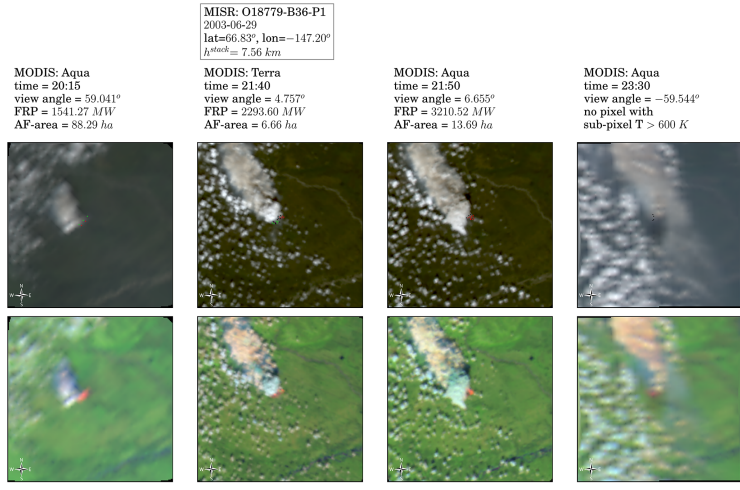
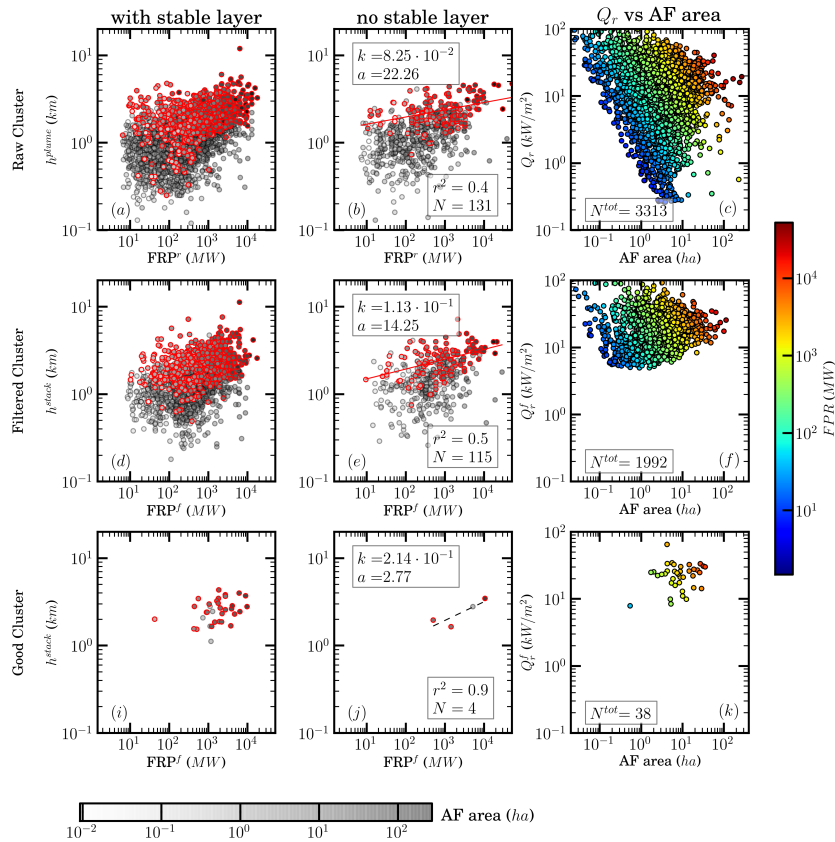


**Figure 6.** Temporal evolution of fire O18779-B36-P1 of the MISR plume height project of (Nelson et al., 2013), as depicted by consecutive MODIS images. Observations are shown from all MODIS overpasses, and for each overpass FRP and AF-area are computed with the dualband algorithm of Dozier (1981) and shown in the top row (see Sect. 4.1), an RGB true colour composite image is derived from the MODIS red, green and blue wavelength bands and shown in the top row, and a RGB IR colour composite is derived from MODIS bands centred at 2.15, 1.24 and 0.6  $\mu\text{m}$  respectively. See Appendix C for an explanation of the simulated NIR colour composite image colours. Each image is 100 km  $\times$  100 km in size, centred on the location of the MISR detected fire plume. The location of fire pixel from the collection 5 MODIS active fire product (Giglio et al., 2003) are also shown in the simulated true colour composite images, using the following colour code, black = sub-pixel effective fire temperature < 600 K, red and green = sub-pixel effective fire temperature > 600 K. Red pixels mark the biggest cluster which is selected if more than one cluster are surrounding the plume (see Sect. 4.1). The details of the MODIS observation times and view angles are included above each image.

9881



9882

**Figure 7.** Relationship between fire and plume observables: FRP, AF-area, FRP density and plume height defined in Sect. 4.1 for the 3 dataset introduced in Sect. 4.2 and based on the North American MISR-derived plume height database of Nelson et al. (2013). **(a)** and **(b)** show, respectively, the relationships between  $\text{FRP}'$  and  $h^{\text{plume}}$  for the fires of the raw cluster data set for atmospheric profiles with and without a stable layer, as was shown previously in (Val Martin et al., 2010). In **(a–e)**, **(i)** and **(j)** points with red color edges correspond to plumes detected above the boundary layer, whilst not circled points come from fire plumes trapped within the PBL. The coefficient of determination ( $r^2$ ) is shown for cases with unstable atmosphere for all fire if the fitted line is dashed black, or only for the fire plumes above the boundary layer if the fitted line is red. For the 3 dataset those in unstable atmosphere always show a higher coefficient of determination than those in stable atmosphere (Val Martin et al., 2010). The right column shows the relationship between FRP density and AF-area as shown in Peterson et al. (2014).

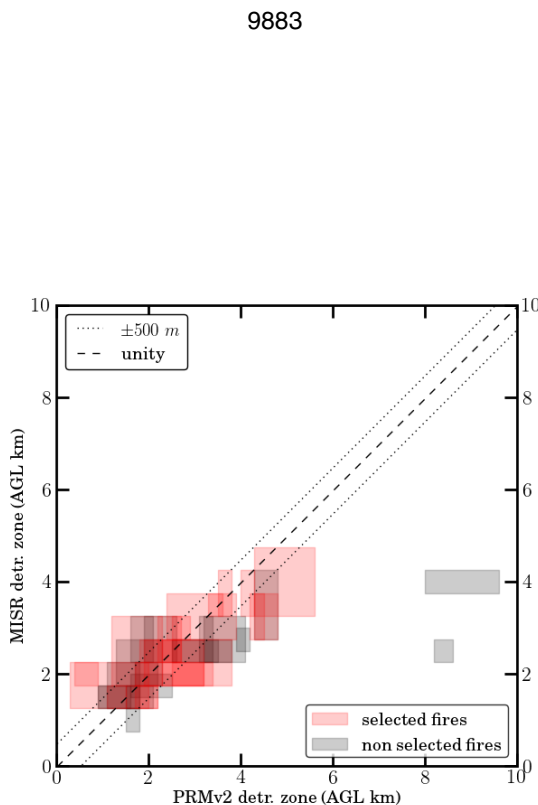


**Figure 8.** One-to-one relationship between fire plume  $\text{InjH}$  layer (“deentrainment zone”) estimated from MISR observations (Sect. 4.1), and the equivalent injection height layer simulated by the PRMv2 Model (Sect. 2.2). Results using the 38 fires of the final training dataset are shown (see Sect. 4.2) and the PRMv2 is run using optimised input parameters  $d_{\text{SA}}$  reported in Table 1. Two fires are seen as outliers from the 1:1 relationship, and these are deselected for further analysis as explained in the main text (Sect. 5.1.2).

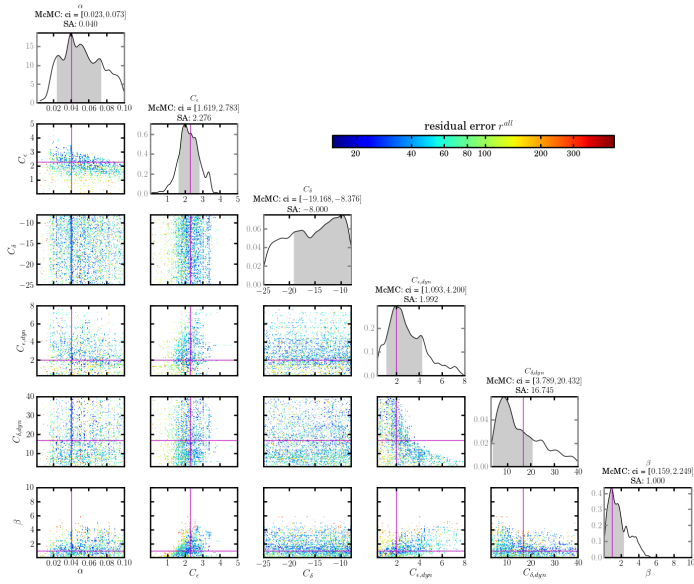
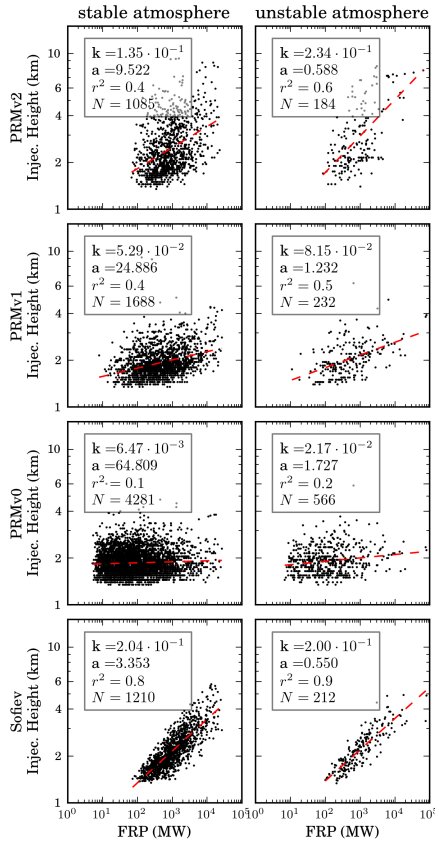


**Figure 9.** Result from the PRMv2 parameter uncertainty test based on the Markov chain Monte Carlo (McMC) algorithm presented in Sect. 5.1.1. The McMC run is based on the observation of the 36 fires selected in Sect. 4.2 (with the two outliers of Fig. 14 removed). Diagonal plots show the Probability Density Function (PDF) of each parameter listed in Table 1. The highest posterior density confidence interval for each parameter is computed from the PDF and are marked in grey. Parameter values established via Simulated Annealing (SA) are reported in purple. Off diagonal plots show the 2-dimensional correlation for each parameter. Points are coloured according to the residual error of the chain element.

9885



9886

**Figure 10.** Relationship between modelled injection height top layer height and FRP, for fire plumes reaching the free troposphere. Fires are those detected by the Collection 5 MODIS Active Fire Product for 2003 over North America (Giglio et al., 2003). As in Fig. 7, fires in stable (left column) and unstable (right column) atmospheres are considered separately. The injection heights are shown estimated using the three versions of the plume rise model considered here (PRMv0, v1 and v2), along with the parametrization of Sofiev et al. (2012). The best fit relationship between plume height ( $h$ ) and FRP ( $h = a \text{FRP}^k$ ) is shown in red. For each plot, fit parameters ( $a, k$ ) and the coefficient of determination ( $r^2$ ) are reported, as well as the number of fires  $N$  which varies since we show results from only plumes that are reported to have heights above the PBL using the particular model under examination. Injection height are reported as height above ground level (km).

9887

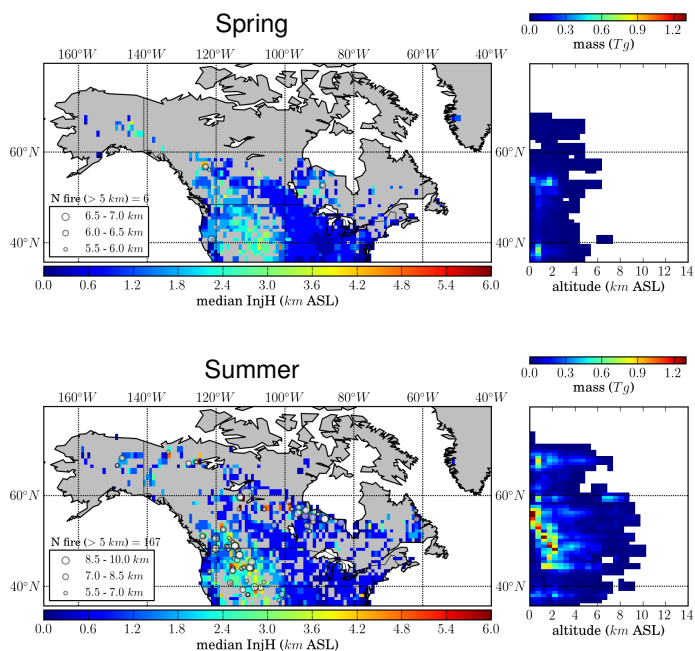


**Figure 11.** Seasonal maps of the distribution of landscape fire smoke plume injection height (InjH) over North America, calculated for the year 2003 from MODIS active fire product data, a simple model of 6 h fire persistence, and the optimised PRMv2 model. Results are shown gridded at  $1.0^\circ$ , with a 500 m vertical grid resolution. For each season, the left column shows the horizontal distribution of the seasonally integrated InjH median (equal fire-consumed mass is located below and above), single fire events having a modelled plume height above 5 km, whilst the vertical distribution of the emissions from the burnt biomass integrated over all longitudes are shown in the right column.

9888

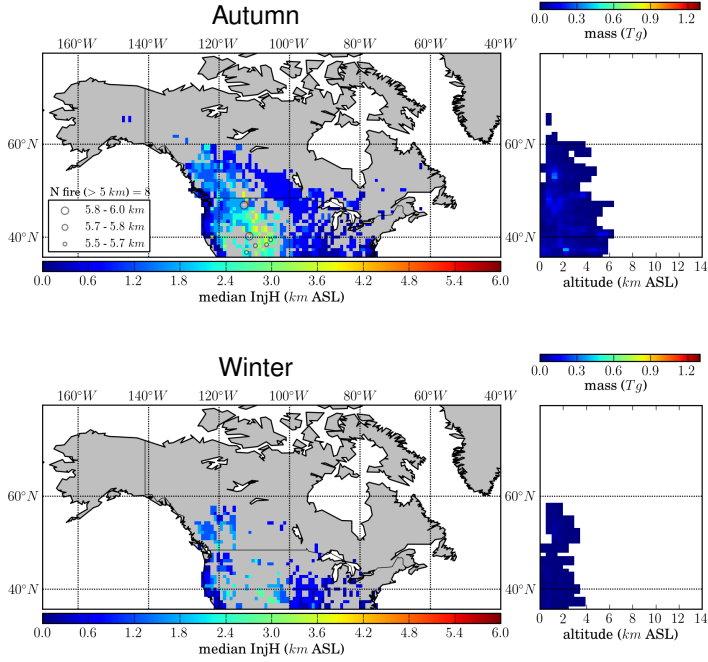


**Figure 12.** Same as for Fig. 11.

9889

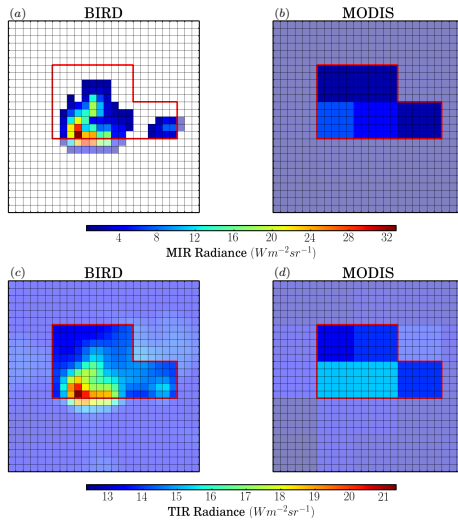


**Figure 13.** Geo-referenced, co-located imagery collected by **(a)** and **(c)** the BIRD satellites 185 m spatial resolution Hotspot Recognition Sensor (HSRS) in the MIR and LWIR bands respectively (Zhukov et al., 2006), and **(b)** and **(d)** the 1 km spatial resolution data collected in the MIR and TIR bands of the MODIS sensor operated on the Terra satellite (Giglio et al., 2003). Data are from a Siberian forest fire observed on the 10 July 2003 ( $57.8873^{\circ}$  N;  $97.7711^{\circ}$  E). See Appendix B for full wavelength specifications of each sensor. Imaging times were 05:32 UTC for BIRD, and 04:55 UTC for MODIS. The red outline shows the fire cluster contour derived from the active fire pixels detected by the Collection 5 MODIS Active Fire and Thermal Anomaly product of (Giglio et al., 2003). In the BIRD imagery, the MIR band only shows pixels detected as fire, while in the TIR band pixels outside the MODIS cluster mask are shaded.

9890

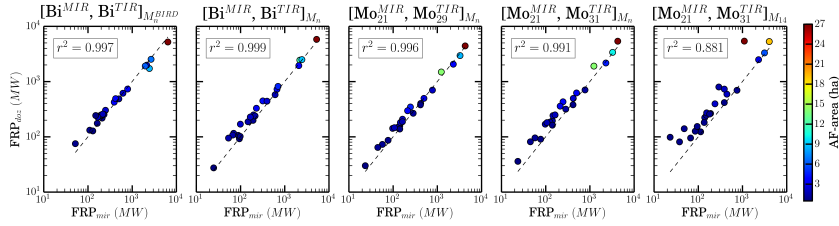


**Figure 14.** Comparison between  $\text{FRP}_{\text{mir}}$  and  $\text{FRP}_{\text{doz}}$  for the 5[sensor<sup>MIR</sup><sub>band</sub>, sensor<sup>TIR</sup><sub>band</sub>]mask selection introduced in the text. The masks ( $M_n$ ,  $M_n^{\text{BIRD}}$ , and  $M_{14}$ ) are different approaches to evaluate fire and background radiance (see Appendix B for more details).  $\text{FRP}_{\text{mir}}$  is retrieved following the approach of Wooster et al. (2005) and  $\text{FRP}_{\text{doz}}$  is directly calculated from the output of the Dozier (1981) algorithm assuming the fire is behaving as a black body.

9891

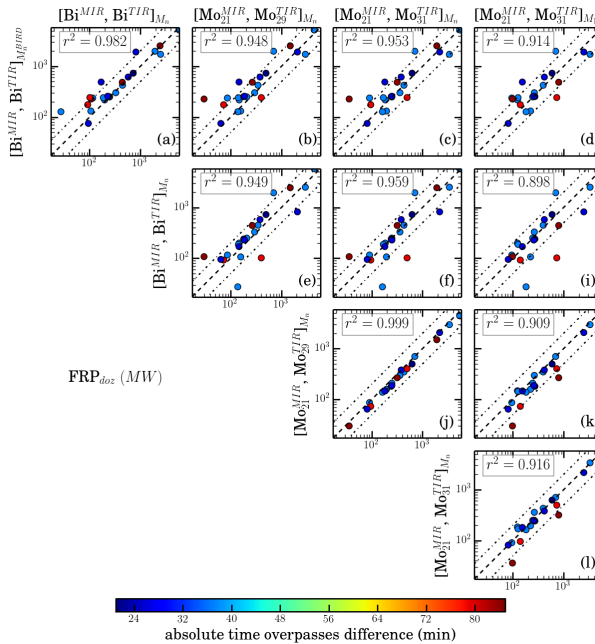


**Figure 15.** Comparison of fire radiative power as derived from active fire effective temperature and area measures output from implementation of the Dozier (1981) fire characterisation approach for 5 sensor and active fire mask combinations introduced in Appendix B.  $\text{FRP}_{\text{doz}}$  derivation is detailed in Sect. 3.3. The dashed lines represent the 1-to-1 relationship, whilst dotted lines show agreement within a factor of 2. The colour of the points represents the absolute overpass time difference between observation of the BIRD satellites Hotspot Recognition Sensor (HSRS) and the MODIS sensor operated on the Terra satellite.

9892

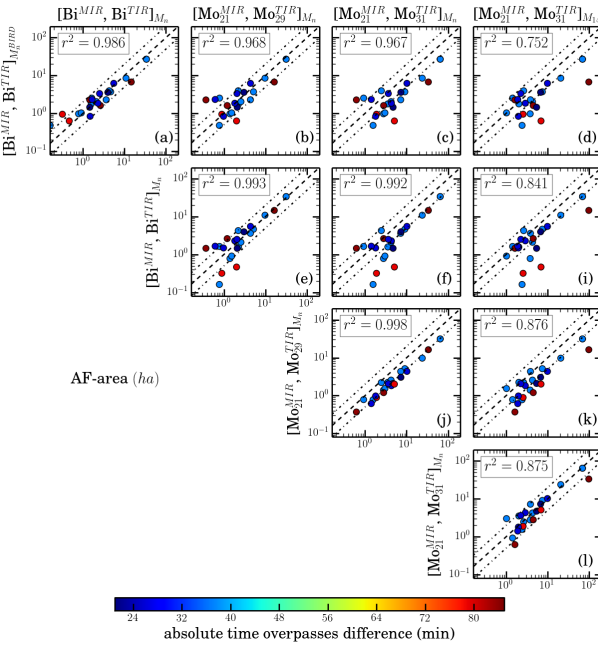


**Figure 16.** Comparison of effective active fire area (AF-area; ha) as estimated from implementation of the Dozier (1981) fire characterisation approach for 5 sensor and active fire mask combinations introduced in Appendix B. AF-area derivation is presented in Sect. 3.2. The dashed lines represent the 1-to-1 relationship, whilst dotted lines show agreement within a factor of 2. The colour of the points represents the overpass time difference between observation of the BIRD satellites Hotspot Recognition Sensor (HSRS) and the MODIS sensor operated on the Terra satellite.

9893

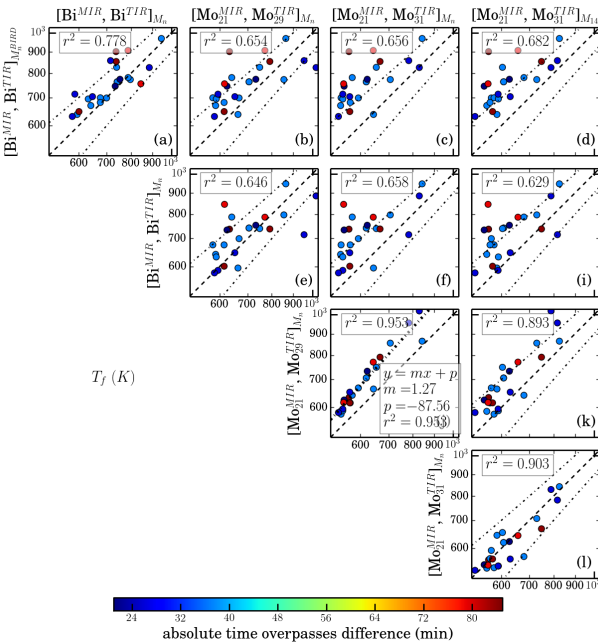


**Figure 17.** Comparison of effective active fire area temperature ( $T_f$ , K) as estimated from implementation of the Dozier (1981) fire characterisation approach.  $T_f$  is shown calculated from the five different sensor and active fire mask combinations introduced in Appendix B. The dashed lines represent the 1-to-1 relationship, whilst except for panel (j) dotted lines show a  $\pm 100$  K interval around this. For panel (j) the dotted lines represent the linear best fit. The colour of the points represents the overpass time difference between observation of the BIRD satellites Hotspot Recognition Sensor (HSRS) and the MODIS sensor operated on the Terra satellite.

9894

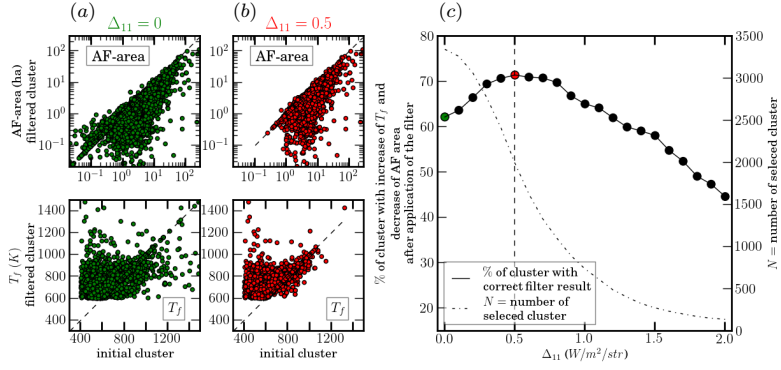


**Figure 18.** Action of the TIR radiance signature test ( $\Delta_{11} = L_{\text{fire}}^{\text{TIR}} - L_{\text{background}}^{\text{TIR}}$  [ $\text{W m}^{-2} \text{ str}^{-1}$ ]) on the Dozier Algorithm response. For two values of the TIR radiance signature test, panels **(a)** ( $\Delta_{11} = 0$ , green) and **(b)** ( $\Delta_{11} = 0.5$ , red) show a 1-to-1 comparison of (i) Active Fire area (AF-area, top) and (ii) fire temperature  $T_f$  (bottom) derived from the North American MISR dataset for fire clusters formed of all fire pixels detected in the Collection 5 MODIS active fire product (MOD14 Giglio et al., 2003) (initial clusters) and filtered fire clusters formed of only MOD14 fire pixels having a sub-pixel temperature  $> 600\text{K}$  (filtered clusters). Panel **(c)** reports the percentage of fire clusters showing a consistent behaviour after application of the low sub-pixel temperature of Sect. 3.2 (i.e. filtered cluster has a higher temperature and a lower area) for values of the TIR radiance signature test ( $\Delta_{11}$ ) ranging from 0 to 2. The total number of selected clusters matching the TIR radiance signature test is also reported (dashed dotted line). The green and red points match information from panel **(a)** and **(b)** respectively.